Thesis for the degree of Doctor of Philosophy
in the Natural Sciences

EFFECT OF MICROWAVES ON MICROTUBULE STRUCTURE AND FUNCTION PROBED BY LIGHT AND X-RAY SCATTERING

Rajiv Harimoorthy

UNIVERSITY OF GOTHENBURG

Department of Chemistry and Molecular Biology
Gothenburg, Sweden
2018

Thesis for the Doctor of Philosophy
in the Natural Sciences

Effect of microwaves on microtubule structure and function
probed by Light and X-ray Scattering

Rajiv Harimoorthy

Cover: A rendition of a Microtubule
(Picture credit: Daniel Sarabi)

ISBN: 978-91-629-0456-2 (Print)
ISBN: 978-91-629-0457-9 (PDF)
Available online at http://hdl.handle.net/2077/55068

Department of Chemistry and Molecular Biology
Division of Biochemistry and Structural Biology
University of Gothenburg
SE-405 30, Göteborg, Sweden
Printed by BrandFactory AB
Göteborg, Sweden 2018

Abstract

We are constantly exposed to radiation in some form or another from our environment. High frequency electromagnetic radiation, including ultraviolet light and X-rays, cause damage to living organisms due to ionization events. Microwaves are known to cause heating and may also induce non-thermal effects in living organisms. It is therefore important to distinguish between thermal and non-thermal effects of microwave radiation and provide evidence for their biological effect. In this thesis we use light scattering to show that microwaves have a non-thermal functional effect on a protein complex called microtubules, which are biological nanotubes that stretch for several microns in length in eukaryotic cells. We also use X-ray scattering to measure whether or not microwaves cause a structural perturbation to microtubules in solution. Finally, this thesis examines the potential of coherent diffractive imaging at an X-ray free electron laser for single-particle imaging of biological fibres, including microtubules.

Acknowledgements

I started this journey towards my PhD almost five years ago and along the way I have worked with some fantastic people both in the lab and during beamtimes abroad. It certainly would not have been possible with the support of several of these people.

One fine summer five years ago, I decided to make a call in the hopes of talking to a German sounding professor. Instead, I was subject to a language I never heard of and it turns out it was a Kiwi on the line. That Kiwi turned out to be **Richard**, my prospective supervisor. I was later invited for an interview to talk about cricket and the like and it turned out well. I still remember the day when you wrote to me ''are you ok working with cow brains?'' Somewhere along the line, probably you presumed that I could be a practicing Hindu, but I was an outlier and accepted to work on the project. It has been a wonderful experience to work on this inter-disciplinary project along with the opportunity to develop independent thinking. I had the opportunity to travel around the world and work with people with different expertise. As this project takes off, I hope it will set a new direction for the lab in the years to come. Thanks for letting me be part of this initiative. Looking back, I think I have developed both scientifically as well as personally. I also do hope NZ will one day lift the Cricket World Cup!

Gisela, though we do not make the brain smoothies together anymore, I do remember the lighter moments when you instilled a sense of reality when I was very optimistic that the brain prep will be done earlier. Somehow, there seems to be an aura of calmness surrounding you and that explains why I kept bursting into your office quite often the last few months. Your advice and guidance on this MT project has been very valuable and of course, it goes without saying, you've been a wonderful co-supervisor!

Martin, thanks for being my examiner and for answering all the numerous questions related to my PhD.

Several people have been involved in this electric field-MT project without whom it would have been almost impossible to accomplish what we have achieved. First, **Greger** and your unfinished coffee's, it's been fun to work with you spending long hours on the brain prep and all the crazy beamtimes we've had. Thanks for the mid-summer and Christmas invitations, I can now sing and dance a little better although a few shots of schnapps still needed. I am sure you will carry the mantle of this MT

project. **Alex,** your input in data analysis and modelling for the MT project has been very valuable.

Christer, the work involved in this thesis certainly would not be possible without your sincerity and dedication. You put in a lot of commitment to this project and worked until your last moments, at times instructing your daughter to perform tasks from your bed. This thesis is a testament to your hard work and the efforts you put in.

During the early days of the project, we were fortunate to get beamtime at Maxlab in Lund. **Roberto,** helped a great deal with the software and answering our calls most of the time, **Marjolein** for granting beamtimes at short notice, **Chris** and **Jie** for all the technical help during beamtimes. Several others contributed to this project including **Peter** and **Amit**. **Per** and **Johanna** for sharing your extensive knowledge on microtubules. I did learn a lot from the many discussions we have had. Also thanks to all the beamline staff at cSAXS and Diamond for all the help during beamtimes.

I also have got to know a host of other wonderful people in the lab with whom I have spent numerous fika breaks or travelled to beamtimes including **Cecilia W**, **Elin**, **Rob D**, **Alex**, **Stefan, Vijay, Petra & Rebecka**. **Daniel,** good luck with the setar and I hope I can watch you play one day. **Giorgia,** thanks for approving my Italian pronunciation. **Cecilia S,** I swear I will not give you names anymore! **Per B** and **Rob B,** thanks for proof-reading my thesis. **Stephan** and **Florian,** I promise I shall one day beat you in Table Tennis.

Rhawnie, my office-mate, thanks for putting up with the annoyance of people barging into the office all the time and good luck with your thesis!

To the Westenhoff group, **Sebastian** I still recall the first beamtime when you ordered us to run to the train in Switzerland only for my bag full of oranges to snap and roll down the train platform, a scene reminiscent of a Bollywood song sequence! **Leo, Elin C, Emil, Linnéa, Mat, Ash, Joakim, Oskar, Petra E** all of you make this corridor lively and fun and for all the happy beer club moments we've had.

Gergely, **Victor & Stanislav**, good luck with the THz project. **Majo,** lets do the Aussie trip again. **Maja,** good luck with your PhD.

Rosie, thanks for being my chauffeur during the last few days. **Kristina, Weixiao**, **Parveen & Swagatha** it's been a pleasure working with you all. To the newbies in the first floor, **Emilie, Darius, Davide, Dmitria** and **Björn,** I'm

sure you all will have a great time ahead.

My previous supervisors **Sandor, Hongyan** and **Lihong** for giving me the opportunity to pursue research in Sweden.

Mike, **Mikae**l, **Alex B**, **Maria**, **Sebastian P**, **Annette**, **Ida** – the lundberg oldies, it's been great knowing you all! **Jennie-** I know your love of spiders, thanks to the Aussie trip! You must be happy coming back home.

Lars and **Bruno** for solving all the hardware and software issues at short notice, sometimes I've asked for help a day before the beamtime and it's done. Thanks for that!

To my friends in Sweden, India and abroad, all of you know who you are and thanks for all the support through these years.

I might not have been in Sweden without the support of these two people. **Mani Iyer,** for having the trust in me and being a guarantor for my education loan, which enabled me to study in Sweden. I'm equally impressed by your decision to leave the corporate world to focus on social initiatives. **Urmish Chudgar,** thanks for introducing us to the west of India and for all the conversations we've had about career and life over the years.

Last but not the least, my parents who have supported me in every possible way and made many sacrifices, sacrifices that I now appreciate much more. For that and ever, I shall be forever grateful.

Contribution report

PAPER I: I designed and executed the light scattering measurements, performed data analysis and contributed in writing of the paper along with my supervisor.

PAPER II: I was involved in planning and designing experiments over several beamtimes, including sample preparation and running the experiments. I analysed the data and produced the figures for the paper.

PAPER III: I produced the protein samples, planned, designed and executed the X-ray scattering measurements along with my supervisor. I did initial data analysis and contributed in the writing of the manuscript.

PAPER IV: I was part of the experiment at LCLS and contributed towards sample injection and delivery. I also made some of the Gas Dynamic Virtual Nozzles (GDVN) used in the experiment.

PAPER V: I purified the proteins, prepared the samples during the experiment and was involved in sample injection and delivery at the LCLS. I also made some of the Gas Dynamic Virtual Nozzles (GDVN) used in the experiment.

PAPERS INCLUDED IN THE THESIS

PAPER I: **Rajiv Harimoorthy**, Guo Chen, Peter Berntsen, Greger Hammarin, Per Widlund, Christer Stoj†, Helena Rodilla, Jan Svenson, Gisela Brändén, Richard Neutze ''Microwave radiation induces non-thermal acceleration of microtubules''. *Submitted*

PAPER II: Amit Sharma, Peter Berntsen, Roberto Appio, **Rajiv Harimoorthy**, Jennie Sjöhamn, Michael Järvå, Alexander Björling, Greger Hammarin, Richard Neutze
'' A simple adaption to protein crystallography station to facilitate difference WAXS studies''. *Submitted*

PAPER III: **Rajiv Harimoorthy***, Greger Hammarin*, Alexandr Nasedkin, Christer Stoj†, Daniel Sarabi, Giorgia Ortolani, Ana Diaz, Viviane Lutz-Bueno, Roberto Appio, Jan Swenson, Andreas Menzel, Gisela Brändén, Richard Neutze. ''Microwave induced structural perturbations within microtubules'' *Manuscript*

PAPER IV: Popp D, Loh ND, Zorgati H, Ghoshdastider U, Liow LT, Ivanova MI, Larsson M, DePonte DP, Bean R, Beyerlein KR, Gati C, Oberthuer D, Arnlund D, Brändén G, Berntsen P, Cascio D, Chavas LMG, Chen JPJ, Ding K, Fleckenstein H, Gumprecht L, **Harimoorthy R**, Mossou E, Sawaya MR, Brewster AS, Hattne J, Sauter NK, Seibert M, Seuring C, Stellato F, Tilp T, Eisenberg DS, Messerschmidt M, Williams GJ, Koglin JE, Makowski L, Millane RP, Forsyth T, Boutet S, White TA, Barty A, Chapman H, Chen SL, Liang M, Neutze R, Robinson RC. ''Flow-aligned, single-shot fiber diffraction using a femtosecond X-ray free-electron laser''.
Cytoskeleton(Hoboken) 2017 Dec; 74(12):472-481. doi: 10.1002/cm.21378

PAPER V: Gisela Brändén, Greger Hammarin, **Rajiv Harimoorthy**, Alexander Johansson, David Arnlund, Erik Malmerberg, Anton Barty, Stefan Bäckström, Peter Berntsen, Daniel P. DePonte, Caroline Seuring, Tomas A. White, Francesco Stellato, Richard Bean, Kenneth Beyerlein, Cornelius Gati, Dominik Oberthüer, Marvin Siebert, Marc Messerschmidt, Garth J. Williams, N. Duane Loh, Henry Chapman, Peter Zwart, Mengning Liang, Sébastian Boutet, Robert Robinsson, Richard Neutze ''Coherent Diffractive Imaging of Microtubules using XFEL radiation'' *Manuscript*

Related papers that I have co-authored but not included in this thesis

PAPER VI: Dods R, Båth P, Arnlund D, Beyerlein KR, Nelson G, Liang M, **Harimoorthy R**, Berntsen P, Malmerberg E, Johansson L, Andersson R, Bosman R, Carbajo S, Claesson E, Conrad CE, Dahl P, Hammarin G, Hunter MS, Li C, Lisova S, Milathianaki D, Robinson J, Safari C, Sharma A, Williams G, Wickstrand C, Yefanov O, Davidsson J, DePonte DP, Barty A, Brändén G, Neutze R. From Macrocrystals to Microcrystals: A Strategy for Membrane Protein Serial Crystallography. Structure. 2017 Sep 5;25(9): 1461-1468.e2.doi: 10.1016/j.str.2017.07.002.

PAPER VII: Nogly P, Panneels V, Nelson G, Gati C, Kimura T, Milne C, Milathianaki D, Kubo M, Wu W, Conrad C, Coe J, Bean R, Zhao Y, Båth P, Dods R, **Harimoorthy R**, Beyerlein KR, Rheinberger J, James D, DePonte D, Li C, Sala L, Williams GJ,Hunter MS, Koglin JE, Berntsen P, Nango E, Iwata S, Chapman HN, Fromme P, Frank M, Abela R, Boutet S, Barty A, White TA, Weierstall U, Spence J, Neutze R, Schertler G, Standfuss J. Lipidic cubic phase injector is a viable crystal delivery system for time-resolved serial crystallography. Nat Commun. 2016 Aug 22;7: 12314. doi: 10.1038/ncomms12314.

PAPER VIII: Björling A, Berntsson O, Takala H, Gallagher KD, Patel H, Gustavsson E, St Peter R, Duong P, Nugent A, Zhang F, Berntsen P, Appio R, Rajkovic I, Lehtivuori H, Panman MR, Hoernke M, Niebling S, **Harimoorthy R**, Lamparter T, Stojković EA, Ihalainen JA, Westenhoff S. Ubiquitous Structural Signaling in Bacterial Phytochromes. J Phys Chem Lett. 2015 Sep 3;6(17):3379-83. doi: 10.1021/acs.jpclett.5b01629

Abbreviations

List of abbreviations I have used in the thesis

cSAXS	coherent **S**mall **A**ngle **X**-ray **S**cattering (beamline at the SLS)
E.coli	**E**scherichia **c**oli (bacterial strain)
EM	**E**lectro**m**agnetic radiation
ESRF	**E**uropean **S**ynchrotron **R**adiation **F**acility
GHz	**G**iga**H**ertz frequency
I911-2	Beamline at MaxII (synchrotron radiation facility in Lund, Sweden)
SAXS	**S**mall **A**ngle **X**-ray **S**cattering
SLS	**S**wiss **L**ight **S**ource (synchrotron radiation facility outside Zurich)
SoPIP2;1	Spinach Plasma Membrane Aquaporin
TR-WAXS	**T**ime **R**esolved-**W**ide **A**ngle **X**-ray **S**cattering
WAXS	**W**ide **A**ngle **X**-ray **S**cattering
XFEL	**X**-ray **F**ree **E**lectron **L**aser (an intense and bright X-ray source)

Contents

Chapter 1

Introduction

1.1 Electromagnetic radiation

Electromagnetic radiation (EM) is a form of energy emitted into space by natural sources such as the sun. Electromagnetic radiation encompasses a broad spectrum of frequencies including infrared light, radio waves to ultraviolet light and X-rays to gamma rays. Some of this radiation emitted mostly by the sun reaches our atmosphere while most of the harmful radiations such as ultraviolet rays are prevented from reaching the atmosphere by the ozone layer. As all types of radiation travel in waves we can measure their wavelength and hence the type of radiation.

Electromagnetic radiation encompasses a broad range of frequencies (Figure 1.1) but electromagnetic radiation in the gigahertz frequency range lies between the super high frequency band (3-30 GHz) and the far infrared band (20 THz to 300 GHz). For the purpose of this thesis most of the work has been done with a frequency of 20 GHz. In the literature several names are employed to describe the same parts of the EM spectrum but for coherence and simplicity, from hereon I refer to the electromagnetic spectrum concerning this frequency as microwaves.

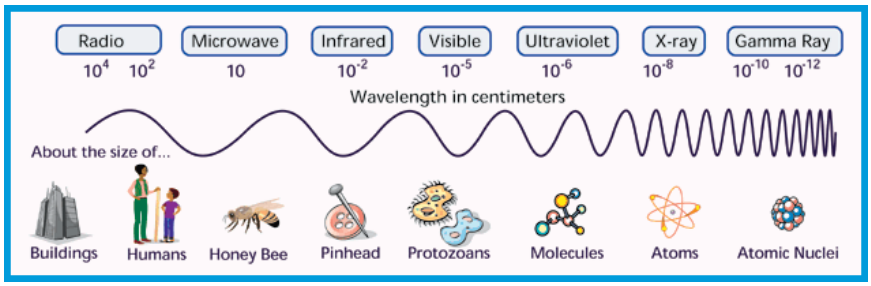

Figure 1.1: Electromagnetic spectrum (Adapted from http://www.space-exploratorium.com/electromagnetic-spectrum.htm)

The energy of GHz photons is several orders of magnitude below that required to ionize or remove valence electrons from biological molecules, which is typically in the order of several electron volts (eVs). Hence these ''G-rays'' or gigahertz waves are referred to as *non-ionizing radiation*. It is important to distinguish between ionizing and non-ionizing radiation because these different domains have different effects on biomolecules. The fundamental difference between ionizing and non-ionizing radiation is that the ionizing radiation carries photons with enough energy to cause ionization effects on water and biomolecules. In contrast non-ionizing radiation does not destroy interatomic bonds and therefore do not lead to chemical transformations.

In 1975, Herbert Fröhlich proposed that energy in cells was not thermalized but instead stored in molecular vibration modes. He hypothesized that coherent dipole vibrations generate an electromagnetic field that is used for long-range interactions[2]. Fröhlich was farsighted in his approach, in that he proposed that biomolecules possess metastable states with high dipole moment. These molecules with high dipole moments could be stabilized by deformations and through displacement of counter ions. There is a possibility that such a molecule will be lifted to its metastable state on application of electric fields[2,3]. This hypothesis is known as the Fröhlich's hypothesis. Subsequent to this prediction several studies have been conducted over the years claiming to either prove or disprove this hypothesis which has been a subject of intense debate.

Radiation in the regime between 30 and 300GHz is used as a non-invasive complimentary medicine against a variety of diseases such as gastric and duodenal ulcers, coronary artery disease, chronic non-specific pulmonary diseases, traumatism and tumors[4-9]. In most of

these studies the most commonly used frequencies in therapy are 35, 42.2, 53.6, 61.2 and 78GHz[10,11].

One interesting application has been the use of low-intensity electromagnetic waves in pain therapy. Clinical trials on the effect of millimeter wave therapy have shown that there are detectable signs of pain relief after several minutes of exposure and lasted for several days[9]. In this study the characteristic feature of the pain-relief effect was due to the immediate onset of analgesia upon application of millimeter waves[9]. Other studies have shown the influence of millimeter waves on the immune system where trials were performed on patients whose immune system was affected[9,12]. However the side effects of such a treatment is still a concern as the claim of several authors that the frequencies of 45.2, 53.5 and 61.2 GHz possess therapeutic effects is not verified by sufficient data[9,13].

Apart from being used in medical applications, these millimeter waves are being used in traffic and military applications and also have expanding applications in the high resolution and high speed wireless technology[10,14]. Due to the increasing usage of this frequency domain in a wide variety of applications, investigations into the biological effect of this radiation have gained more interest.

1.2 Why study the effect of electric fields?

Oscillating electric fields at certain frequencies, especially in the range of 30 and 300 GHz are known to cause an increase in cell temperature, thereby hindering or influencing biological processes such as cell growth. Apart from the temperature related changes, there is thought to be a second kind of biological effect on exposure to electric fields although the literature is contradictory at this point [15-17].

To test the non-thermal effect on biological subjects several experiments have been performed, in particular between the megahertz to terahertz frequencies since they are used in a wide range of industrial and domestic applications[18-20]. In a very early study conducted by Devyatkov in 1974, he showed that low- intensity radiation between 39-46 GHz when applied on yeast culture promoted the growth of the colony[21]. In this study he concluded that the effect of millimeter wave radiation was frequency dependent as well as on the time of exposure and most importantly it was claimed that the applied power had a weak effect. Another study showed suppressive effects in *Escherichia coli* when the culture was exposed to millimeter waves for 1 hour each day for several days[22]. Similar

suppression effects were observed in other bacteria such as *Clostridium sporogenesis* and *Clostridium histoliticum* and showed a decrease in size and alterations in metabolism[23]. These results have been disputed by researchers in other laboratories.

A more recent study (2013) to verify the Fröhlich theory, was performed to evaluate the effect of terahertz radiation in human cells where the cells were exposed to time periods of up to 6 hours and multiple 3 hour periods and evaluated over several days. The results showed that human epithelial cells and embryonic stem cells were unaffected by terahertz radiation[24]. By contrast in another study by Bock et al[25] on mouse stem cells which were subjected to long-term (> 9h) exposure at 10 THz it resulted in altered levels of gene expression which eventually led to cellular reprogramming.

Both the recent results and those collected in the early part of the 70's both show the inconclusive nature of the research. This could be due to several factors associated with the choice of measurement techniques, choice of organism, molecular composition of the cell and on the parameters of the electromagnetic field itself.

1.3 Possible interaction of electric fields with proteins in solution

Proteins are biological macromolecules comprised of one or more polypeptides. They play many critical roles and are required for the structure, function and regulation of different cells and tissues in the body. Their biological activity sometimes depends on their conformational state. Changes in protein conformation may affect their function and several downstream processes such as signaling pathways, recognition of different molecules, cell proliferation etc. Several factors can affect or alter the conformational state of a protein, such as changes in the temperature, pH or conductivity (measure of a solutions ability to conduct electricity). This may cause the protein to lose its native conformation and unfold the polypeptide chain. Since protein function is tied to its structure (although there are recent reports of disordered proteins with function[26,27]) protein unfolding has debilitating effects on several cell functions.

Electric fields could interact with biological matter through several means. They may act on atoms, ions, molecules, water, proteins, membranes and cells. These may be stand-alone interactions or combined effects. The extent and mechanisms by which electric fields

initiate these interactions and the energy required to affect biological processes is a subject of intense debate and speculation[28-30].

An electromagnetic field acting on any particle or point in space and time can be described by two vectors *E* and *B.* These vectors are defined as the measurable strength of the electric field and magnetic flux density respectively. The force acting on a charged particle due to an electric field is called Coulomb force; while the force due to magnetic flux acting only on moving charges particles is called Lorentz force. When two oppositely charged particles, positive and negative, are separated by a small distance it results in an electric dipole. Similarly, a magnetic dipole arises due to the movement of charges in a closed loop. All these forces may act or influence the arrangement of charged particles.

A system consists of a specific number of positively charged protons and negatively charged electrons. The charge separation within this system results in an electric dipole moment. When an external electric field is applied to a charged particle, the dipoles experience a torque resulting in rotation. This rotation of dipoles expends energy which produces heat due to friction with other atoms. Hence, dipoles align with external fields thereby resulting in the alignment of molecules.

Proteins contain distinct magnetic and electric dipole moments which interact with external fields. Externally applied fields could act on the charges held by a protein[31]. There are theoretical predictions and experimental results showing changes in protein confirmation[32,33] when an external field is applied. Studies on β- lactoglobulin protein by Bohr et al.,[34] have shown that alternating electric fields at 2.45GHz enhances the kinetics of the folding process of globular proteins and they claim that it is a non- thermal effect. It was postulated that the cause of this effect could be excitation of collective intrinsic modes in the protein. It was also shown by Copty et al.,[35,36] that the effect of microwaves on the fluorescence of green fluorescent protein was far greater than could be explained solely by heating. A study by Porcelli et al[37]., on enzymes shows non-thermal irreversible inactivation after exposure to 10.4 GHz microwave radiation. There are also reports of electric field slowing down refolding in myoglobin due to microwave exposure[38]. Studies that claim low-intensity electric fields can induce non-thermal heat shock response in *Caenorhabditis elegans* were retracted[16,39] due to power loss within the Transverse Electromagnetic (TEM) cell resulting in warmer temperatures than the controls[15].

1.4 Cytoskeleton

The cytoskeleton is an important component of cells universally present in prokaryotes, eukaryotes and archaea (Figure 1.2). It provides structure to the cell and helps maintain its shape and internal organization while also providing mechanical support to the cell. The cytoskeleton contributes to the cellular architecture and transport system by governing large-scale cell organization and providing communication lines extending throughout the cell. Apart from its role in transporting different cellular components, the cytoskeleton is involved in many cell-signaling pathways, uptake of extracellular material, cellular migration and plays a vital role in segregating chromosomes during cell division. However, role and structure of cytoskeleton can vary greatly depending on the organism, cell type and cell cycle stage.

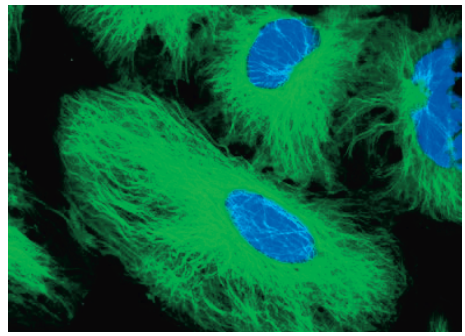

Figure 1.2: Microtubules of an eukaryotic cell labelled with GFP (green); nucleus is stained blue (Adapted from http://lifeofplant.blogspot.se/2011/05/cytoskeleton.html)

The cytoskeleton is comprised of a network of several different components working together to perform a wide variety of tasks in the cell. These components comprise three different filamentous macromolecular protein structures namely microtubules, microfilaments and intermediate filaments. Microfilaments, the narrowest of the three filaments, are fine thread-like fibers mainly composed of actin. Actin is the most abundant cellular protein; it is essential in endocytosis, cellular motility and also responsible for contraction in muscle cells. Intermediate filaments are usually strong and rope-like structures which work in tandem with microtubules providing tensile strength to these delicate structures. Microtubules, the thickest type of the cytoskeletal fibers, are the focus of this thesis and are described below.

1.4.1 Microtubule structure and function

Microtubules are rigid hollow fibers, approximately 25nm in diameter and can grow as long as 50 µm. They are composed of a globular protein called tubulin. Microtubules are polymers, the repeating subunit being a dimer of α- and β- tubulin proteins. While distinct these tubulin proteins nevertheless have extremely similar tertiary structures and a high degree of homology across species[40]. Longitudinal polymerization of tubulin dimers forms protofilaments which in vivo usually interact laterally to form an assembly of 13 protofilaments as shown in Figure 1.3. The protofilaments are arranged in a parallel manner and are polar structures with two distinct ends: a fast- growing plus end and a slow- growing minus end[41-43].

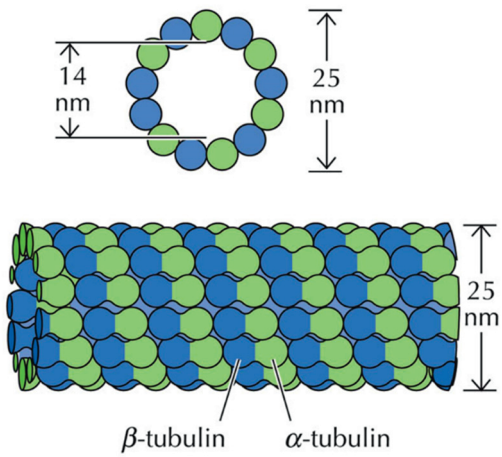

Figure 1.3: Structure of a microtubule (The cell, Fourth Edition, Figure 12.42) © 2006 ASM Press and Sinauer Associates, Inc

1.4.2 Microtubule Dynamics

Tubulin dimers can polymerize and depolymerize in favorable conditions[43]. Therefore, microtubules can undergo rapid cycles of assembly and disassembly as shown in Figure 1.4. Guanosine 5'-triphosphate (GTP) has been shown to regulate microtubule polymerization. While both α and β tubulin monomers can bind GTP but only GTP bound to β-tubulin is hydrolyzed to GDP shortly after assembly. GTP hydrolysis on the tip of a microtubule reduces the binding affinity of tubulin to new dimers and increases tubulin dissociation rate resulting in depolymerization. This dynamic behavior in which tubulin dimers bound to GDP are rapidly lost from the

minus end and replaced by new tubulin dimers with GTP to the plus end contributes to one dynamic feature of microtubules known as treadmilling. This can be modified *in vivo* by proteins that bind and either stabilize or destabilize either end. The second and defining dynamic feature of microtubules is called 'dynamic instability' and is a result of a special property of the microtubule plus end, first reported by Tim Mitchison and Marc Kirschner in 1984[42]. When a tubulin subunit is incorporated to the plus end, GTP is eventually hydrolysed. This hydrolysis is thought to change the tubulins structure such that lateral interactions with neighboring protofilaments are less favored, resulting in strain in the microtubule lattice. However, a stabilizing region of GTP tubulin remains at the plus end, known as a microtubule cap, which prevents depolymerization. This cap is stochastically lost in individual microtubules, resulting in a rapid depolymerization event known as a 'catastrophe.' Because of this property, shrinking microtubules can exist in a population of microtubules that are mostly in a growing phase. Dynamic instability can also be modified by proteins that interact with microtubules. Furthermore, numerous drugs bind tubulin and modify its assembly properties. This interference can stop the cell's cycle which eventually results in apoptosis.

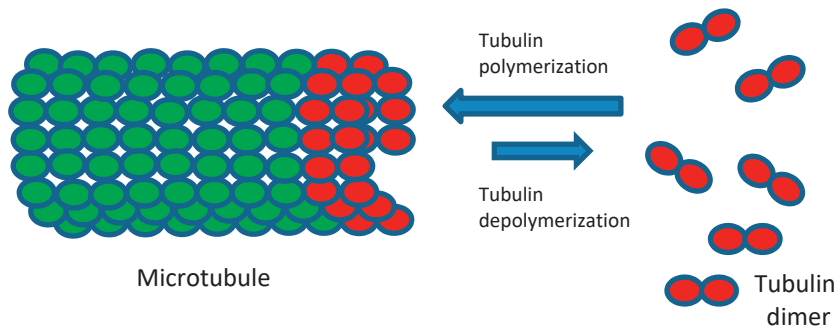

Figure 1.4: Tubulin polymerization and depolymerization

1.5 Synchrotron and XFEL radiation

To study microtubules, you need powerful sources of X-rays. Electrons travelling close to the speed of light can emit synchrotron radiation when their direction of motion is changed by a magnetic field. Utilizing synchrotron radiation requires particle accelerators that can both accelerate the electrons close to the speed of light and use large

magnets to change their direction. A circular 'ring' design allows X-rays to be generated at each shift in direction and every time the electrons circled this ring. Since the electrons are 'stored' within this ring it is called the storage ring. The first generation synchrotron facilities were developed in the 1960's. Since then technological developments in X-ray generation increased the intensity and brilliance of these sources enabling biomolecules to be studied in atomistic detail.

In the second generation synchrotron sources, radiation was produced by both bending magnets and high magnetic devices known as wigglers. Further advancements in technology and optimization of these magnets or wigglers saw them placed in straight sections of a storage ring. The resulting increased brilliance resulted in the third generation and current synchrotron sources such as the European Synchrotron Radiation Facility (ESRF) in Grenoble, Advanced Photon Source (APS) in Chicago and the Swiss Light Source in Villigen. MAXIV Laboratory in Lund, Sweden is the next version of synchrotrons and so is a 3.5 generation facility. Along with the development of the light sources, advancements in detector technology have made it possible to obtain faster read-out times and better image resolution.

Part of the work described in this thesis (**PAPER III** and **PAPER II**) involves work carried out at Swiss Light Source and MAX II (decommissioned) in Lund which is now upgraded to a 3.5 generation facility which will be one of the brightest sources of its kind. The work carried out in this thesis required the use of such X-ray sources due to their high flux and brilliance.

To image a polymer like microtubule which is used in this thesis, the quality of the light source is also important as well as getting as much light as possible on the sample per unit area and time. Furthermore, a stable X-ray source is crucial to obtain accurate data in difference WAXS experiments and it is possible because of the availability of synchrotron sources.

Another focus of this thesis requires the use of fourth generation light sources called X-ray Free Electron lasers (XFELs). XFEL's are a billion times brighter than synchrotrons and also have different properties. XFEL's can provide coherent femtosecond pulses that contain 10^{11}-10^{12} photons per pulse focused to ~1µm spot size.

X-FEL's enable us to take atomic scale motion picture of a chemical reaction in time scale of a few femtoseconds (1 fs=10^{-15} sec) or to unravel the complex molecular structure of a single protein or virus. The extreme peak brilliance coupled with the short pules lasting just few tens of hundreds of femtoseconds in duration enables us to visualize ultrafast protein structural dynamics on the femtosecond-to-picosecond time scales. Furthermore, a major goal of XFEL is to produce atomic level resolution of single particles, although no structure has yet been determined. Another important breakthrough accompanying XFEL development are the advancements in detector technology. The Cornell-SLAC Pixel array detector (CSPAD) is an integrated hybrid pixel array detector at the coherent X-ray imaging (CXI) beamline at LCLS[44,45]. The CSPAD detector has been used in many experiments involving serial femtosecond crystallography and time resolved solution scattering[45-51]. The European XFEL which is expected to be commissioned in early 2018 will have a repetition rate of 27 kHz[52] and to capture this train of pulses, detectors like the Adaptive Gain Integrating Pixel Detector (AGIPD) for single particle imaging and the Large Pixel Detector (LPD) for Femtosecond-X-ray experiments have been developed which will have a repetition rate of 4.5 MHz[53]. These advancements in XFEL technology creates new opportunities in not only life science but also in other branches of science from material physics to study the extreme states of matter such as plasma to chemists studying the dynamics of bond breakage[54,55].

One problem associated with XFEL radiation is that the energy is so high that the X-ray dose delivered to a protein sample from a single shot will destroy the sample before an entire dataset can be collected or a series of meaningful rotations performed to obtain interpretable data. However, before the crystal explodes, it will produce a meaningful diffraction pattern. *Neutze et al.,* in 2000 performed molecular dynamics simulations to demonstrate there was a lag time on the order of femtoseconds after initial X- ray dose before the protein structure has time to respond and reflect the radiation damage[56]. This is called ''diffraction before destruction'' and forms the basis for structural biology experiments at an XFEL[47].

Small- and wide-angle X-ray scattering (SAXS and WAXS) are two powerful techniques that are used to study the structural dynamics of proteins in solution. Both SAXS and WAXS are used to measure non-crystalline samples, thereby alleviating the need to have a protein crystal which can sometimes take years to obtain. SAXS provides

structural information in the small angle (~0.3-4°) region of the scattering pattern providing information in the low resolution (10Å – 250Å) directly related to the shape and size of the molecule. SAXS experiments typically require relatively small amounts of protein sample but require a homogeneous dilute solution in a near physiological buffer. SAXS makes it possible to investigate large protein complexes and intermolecular interactions including assembly in real time[57]. There have been major improvements in data collection routines, modern detectors offering better signal-to-noise ratio and also the possibility to perform time-resolved studies[58]. Data analysis has vastly improved with user friendly software packages available for structural reconstruction from the one dimensional SAXS profile[59-61].

WAXS, similarly to SAXS, produces a diffuse scattering pattern but at wider angles (~3 - 20°). However the WAXS regime scatters X- rays to a much smaller extent than the SAXS regime and hence requires high concentrations of protein sample. The distance from the sample to the detector is shorter and therefore the diffraction maxima at larger angles are observed. With the advent of third generation X-ray sources which are capable of providing high energy X-ray beam has led to solving structures to high resolution (~2.5Å)[62] in combination with other techniques. WAXS is a complimentary technique to crystallography and NMR and can be used indirectly to test structural models, identification of structural similarities and possibly identify novel folds within proteins[63].

1.6 Scope of the thesis

In this thesis, I have used light to study the effect of microwaves on tubulin polymerization and X-ray scattering to study if there are any structural effects on microtubules on exposure to microwaves. I have also used X-FEL radiation to perform coherent diffractive imaging on fibers and filaments.

In **Chapter 2** I introduce the methodology of the different techniques used in this thesis.

In **Chapters 3-6** will form the core of the thesis where I describe in detail about the different results obtained through this work.

Chapter 3 describes the measurements done to show the effect of microwaves on the growth of microtubules using light scattering.

Chapter 4 describes the adaption of a crystallography beamline to perform difference WAXS measurements.

Chapter 5 describes our efforts in understanding the structural perturbations on microtubules on exposure to microwaves using X-ray scattering. **Chapter 6** describes X-ray imaging of microtubules and other filamentous systems at an X-ray Free Electron Source.

Chapter 7 aims to provide a summary and conclude the results of the work described in the thesis and provides future perspectives on the work to be carried out.

Chapter 2

METHODOLOGY

2.1 Purification of tubulin from native sources

Solution scattering experiments in synchrotrons and XFEL's consume large amounts of purified protein ranging from milligrams to grams. In order to produce such large quantities of protein a robust purification protocol that gives high yields is required. Most of the proteins targeted for structural biology studies are expressed in very small quantities in the native host system, thereby necessitating overexpression in different expression systems such as *E.coli*, yeast or mammalian cells. However, tubulin can be efficiently produced and purified directly from animal brain tissue. The purification protocol involves repeated cycles of temperature-dependent tubulin polymerization–depolymerization to obtain functional tubulin dimers[64,65]. The tubulin purification protocol used to carry out the work in this thesis involves a slight modification to the protocols of Borisy et al.,[64] and Howard et al.,[65] which required the use of a MES-based buffer to better depolymerize tubulin and high- molarity PIPES buffer for the polymerization step[66]. The use of high-molarity PIPES results in efficient assembly of microtubules while also preventing contaminating proteins such as MAP's from attaching to microtubules. For each batch of tubulin purification 1kg of bovine or porcine brains were used, corresponding to 5- 10 brains.

Brains

Calf and Porcine brains (Figure 2.1A) were collected from a local slaughterhouse, preserved in ice-cold PBS (20 mM Na-phosphate, 150 mM NaCl, pH 7.2) before use and used as soon as practically possible.

Tubulin preparation

Figure 2.2 shows schematically the tubulin purification protocol. Brains which were preserved in PBS-ice for the duration of transport are cut into small pieces, weighed and transferred to a blender (Figure

2.1). Cold (+4°C) depolymerization buffer (DB) was added at a ratio of 1liter/kg of brain tissue. The mixture was homogenized two to three times for a duration of approximately 30 seconds (Figure 2.1B). The homogenates were then centrifuged in a Beckman JLA 8.1 rotor at 7000 rpm at 4°C for 20 min. The supernatants were pooled (~0.5 l from 1 kg brain) and subjected to another round of centrifugation in a Beckman JA 14 rotor at 14,000 rpm at 4°C for 80 minutes to remove the remaining tissue debris. The supernatants from this centrifugation step were again pooled and supplemented with an equal volume of warm 37°C high-molarity PIPES buffer (HMPB), ATP (1.5 mM final) and GTP (0.5 mM) final. ATP is included in this step to remove the motor proteins and other microtubule-associated proteins (MAPs) which dissociate from microtubules in an ATP-dependent manner[66,67]. Along with the addition of HMPB buffer and nucleotides and an equal volume of pre-warmed 37°C glycerol was added to the solution. The mixture was rapidly brought to 30°C by swirling under hot tap water and then incubated in a water bath at 37°C for 1 h. The polymerized tubulin was then centrifuged in a Ti 45 Beckman rotor at 151,000g (44,000 rpm) for 30 min at 37°C. The resulting microtubule pellets were resuspended in 100ml cold depolymerization buffer and left for 30 min on ice. The depolymerized tubulin was then centrifuged in a Ti 45 Beckman rotor at 70,000g (30,000 rpm) for 30 min at 4°C which is the first cold spin. The supernatant from this centrifugation step is mixed with an equal volume of HMPB supplemented with ATP and GTP, followed by the addition of glycerol as described above. The mixture was incubated in a 37°C water bath for 30 min and the polymerized tubulin was pelleted in a Ti 45 Beckman rotor at 151,000g (44,000 rpm). Following centrifugation, the microtubule pellets were resuspended in 6-7 ml of ice cold General Tubulin buffer and then incubated for 10 min on ice. After this depolymerization step the tubulin in centrifuged in a Ti 70 Beckman rotor at 104,000 g (50,000 rpm) for 30 min at 4°C, which is the second cold spin. The tubulin supernatant was collected and snap-frozen in different sized (200 µl, 500 µl or 1000 µl) aliquots in liquid nitrogen.

Protein concentration

The final tubulin concentration was determined at A_{280} using an extinction coefficient of 115,000[66,68]. Tubulin concentration was measured in triplicates of different dilutions (10X, 20X and 40X) and the final yield from 1 kg of brain tissue was ~250-300 mg. In this thesis, for **PAPER I** we used commercial bovine tubulin purchased from

Cytoskeleton and for the solution scattering measurements (**PAPER III & PAPER V**) we used in-house purified bovine and porcine tubulin.

Figure 2.1: (A) Fresh porcine brains; (B) Homogenized mixture of the brains in a mixer.

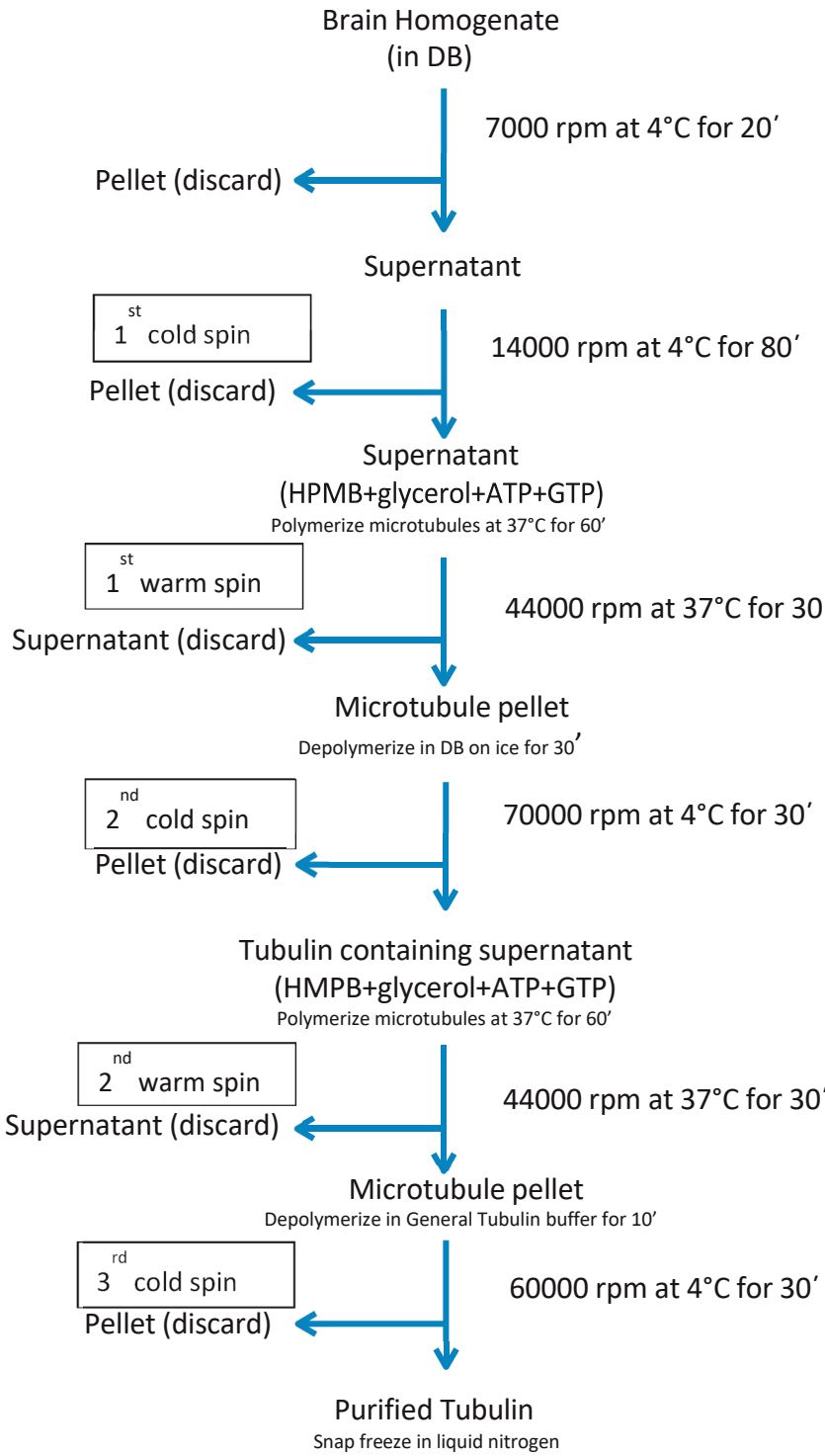

Figure 2.2: Flow-chart illustrating the preparation of pure tubulin: the overall duration of the tubulin purification is between 10 and 12h.

2.2 Light scattering studies of microtubule polymerization

In order to understand microtubule assembly, it is important to understand the pathway which leads to the formation of a microtubule from individual subunits. The focus of *in-vitro* studies has been to understand the mechanism of the assembly during each phase in the growth of a microtubule.

Microtubule assembly *in-vitro* can generally be described as comprising three phases, nucleation, elongation and saturation. During the first phase of nucleation, a new microtubule end or oligomer is formed spontaneously from free tubulin subunits. This initial stable part of the microtubule is called a nucleus. The nucleus can be defined as the first polymer whose growth is thermodynamically stable but the least stable in the entire pathway[69]. If the nucleus is large enough to be stable, the polymerization of tubulin subunits happens along one end of the nucleus resulting in microtubule elongation. Elongation continues until the free tubulin subunit pool is reduced to the concentration in equilibrium with microtubules. Nucleation plays a significant role only in the earlier part of microtubule formation, when the concentration of the free tubulin subunits is highest[69].

The microtubule, although a helical polymer, begins with a formation of a small sheet comprising few protofilaments and grows longer and wider until it reaches a full component of thirteen protofilaments. This is the final stage of the polymerization process at which points it goes from a two- dimensional polymer to an intact helical microtubule. This model of microtubule assembly is widely agreed and independently verified across several labs[70,71].

A simple experiment to measure the kinetics of microtubule assembly is to monitor changes in solution turbidity (optical density). An increase in incident light scattering is observed as the microtubules form with a corresponding increase in optical density. As such, a light source emitting UV-light greater than 320 nm can be used to probe the polymerization process. Below 320 nm the absorption of light by protein and the buffer solution become dominant[72]. We used a UV light source at 365 nm and applied microwaves to check if there is any effect on tubulin polymerization which is the focus of **PAPER I** and is further described in **Chapter 3**.

2.3 Solution scattering at synchrotron sources

Crystallography remains the primary method of choice for solving high resolution structures in structural biology. However, crystallizing proteins and their complexes is both challenging and time consuming. Solution scattering, even though a low resolution technique, is relatively easy as it only requires purified protein sample in solution and enables retrieving structural information of proteins in their near physiological state.

In solution scattering the randomly oriented molecules give rise to a diffuse diffraction pattern as shown in Figure 2.4.

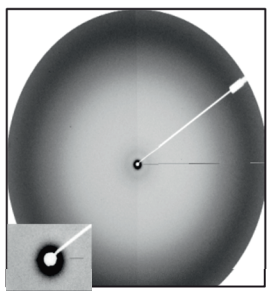

Figure 2.4: A typical solution scattering image; (inset) scattering at low angles with the beamstop in the centre

The intensity of the X-rays can be expressed as a function of the the scattering vector *q,* resulting from a photon of wavelength λ, scattering from the protein sample at an angle 2θ.

$$q = \frac{4\pi \sin(\theta)}{\lambda} \qquad (1)$$

The scattering from a protein solution is the contribution from all atoms present in the system including the solvent. To isolate the scattering only from the protein molecules the scattering from the solvent must be subtracted from the total scattering profile.

The total scattering from all the components in a protein solution can be summed up by the formulae;

$$F(q) = \sum_j f_j \, e^{iq.rj} \qquad (2)$$

where *F(q)* is the amplitude of the scattered wave as a function of *q*, f_j the

atomic form factor and *rj* the position vector of an atom *j.* The atomic form factor *fj*, represents the shape of the molecule or the interference pattern which provides direct information about the size of the molecule. The total absolute scattering is comprised of three parts; the scattering from protein, scattering from the bulk solvent and the scattering from the excluded volume that the protein occupies. In experiments involving protein solutions the majority of the scattering is from the bulk of the solvent (including the capillary) and must be subtracted from the total scattering as described above to obtain any meaningful information about the protein molecules being studied.

In simple terms the scattering from the protein can be calculated with this expression;

$$S_{prot} = S_{obs} - S_{cap} - (1 - v_{ex})\, S_{solvent}$$

where S_{obs} is the scattering from the protein sample; S_{cap} is the scattering from the capillary; v_{ex} is the scattering from the solution (excluded volume) occupied by the protein. $S_{solvent}$ can be calculated by,

$$S_{solvent} = S_{bkgd} - S_{cap}$$

where S_{bkgd} is the scattering from the capillary filled with buffer.

In solution scattering, as opposed to diffraction from a crystal, the individual protein molecules have different orientations which give rise to different scattering properties. To account for the rotational average, the scattering intensity can be explained by the Debye formula,

$$S(q) = N\langle |F(q)^2| \rangle = N \sum_i \sum_j (f_i - \rho_s v_i)(f_i - \rho_s v_j) \frac{\sin(qr_{ij})}{(qr_{ij})} \qquad (3)$$

where *S(q)* is the total scattering from the vector *q*, *N* is the number of the molecules in the system, *rij* is the distance between the atoms *i* and *j*. (f_i - ρ_S v_j) is the difference in amplitude between the solvent and protein atom *j.* The Debye formula can be used to calculate the scattering from a known atomic structure of a protein. However, atomic coordinates for a protein cannot be calculated from a solution scattering experiment as several different structural fits are possible from the measured absolute scattering. This happens to be one of the limitation of solution scattering studies, as it works best only when working on a protein of known structure.

2.3.1 Small Angle X-ray Scattering

SAXS can be used to determine the radius of gyration (Rg), low resolution molecular envelopes and the pair distribution function. Rg gives information about the molecular weight of the protein in solution[73,74]. More structural information about the oligomeric state and complexes can be obtained by performing *ab-initio* shape determinations[75,76]. The pair distribution function provides information regarding the placement of subunits and the nature of structural movements during protein function which could be induced by ligand binding or other changes in the sample environment. Comparing SAXS to known crystallographic structures could give new insights about the behavior of protein in solution, for instance, the unfolding of proteins in solution[63].

A SAXS experimental profile has three distinct regions from which information can be retrieved; Guinier, Fourier and Porod as shown in Figure 2.5.

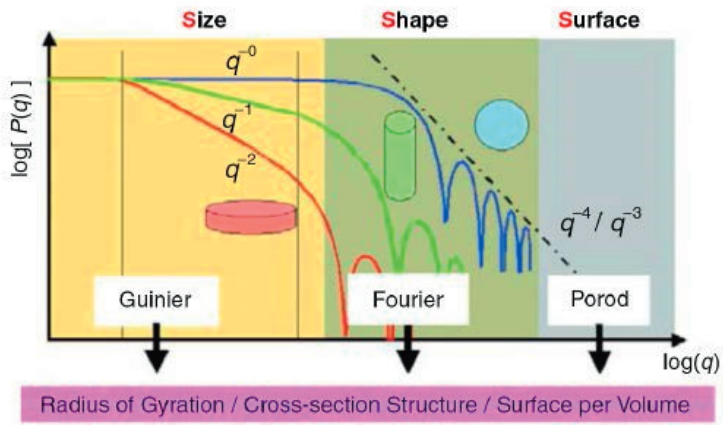

Figure 2.5: Regions of SAXS profile and corresponding data obtained from each region[1] .

From the Guinier region information concerning the radius of gyration (Rg) can be obtained. Rg can be calculated by fitting a line to the natural log of the intensity as a function of the square of the scattering vector q^2[1]. Several factors affect the radius of gyration such as aggregation of molecules, polydispersity or the improper subtraction of buffer.

In the Fourier region, information regarding the shape of the particle can be obtained by determining the pair distribution function. The pair distribution function tells us the distribution of the distances between pairs of particles contained within a certain volume. In the case of protein solution scattering it refers to the distribution of electrons averaged over a radius. The formula below is used to obtain the general particle shape, provided all the particles are in a similar shape.

$$\rho(r) = \frac{1}{2\pi^2 r}\int_0^\infty qP(q)\sin(qr)\,dq \qquad (4)$$

The porod region, provides information regarding the surface, such as the surface to volume ratio for the particles in solution Equation (6). The porod invariant can also be determined which is independent of the concentration and directly proportional to the molecular mass Equation (5).

$$Q = \int_0^\infty q^2 I(q) dq \qquad (5)$$

where *Q* is the Porod invariant, *I* is the intensity and *q* is the scattering vector.

$$\frac{S}{V} = \frac{\pi(\lim_{q\to\infty} I(q)q^4}{Q} \qquad (6)$$

A Porod plot provides information regarding the Porod volume and also the molecular weight of particles at high *q* values[77,78]. The Kratky plot is used to analyze the confirmation of proteins. It is usually used to identify disordered states and distinguish them from globular states using the formula (*I(s).s*^{2} *versus s*), where *I* corresponds to intensity and *s* corresponds to the scattering vector[78].

2.3.2 Wide Angle X-ray Scattering

The WAXS region corresponds to scattering angles comparable to those in crystallographic studies (q ~ 2.5Å^{-1}). The extension of the scattering angles to higher *q* enables us to obtain information regarding the secondary (alpha helices and beta sheets) and tertiary structure of the proteins. However, as one goes higher into the WAXS regime the intensity of the scatter is 1-3 orders of magnitude weaker than the scattering obtained from the SAXS regime. Since the information obtained in solution scattering is approximately linear in *q*, WAXS has several times the amount of information contained in a SAXS pattern[63].

WAXS is a powerful method when combined with crystallography since it is possible to calculate WAXS patterns from atomic coordinates and also to test detailed molecular models of a system. Rapid progress has been made in developing algorithms and software for calculating solution scattering patterns from atomic coordinates. One of the most widely used programs for calculating solution scattering patterns CRYSOL, has provided with the capability to perform *ab-initio* shape determination[75,76,79]. CRYSOL, per se, works very well and is adequate for calculating SAXS patterns but the approximations involved introduces errors when calculating scattering patterns at wider angles[80] but works very well when the parameters involved in defining the solvation layer and the excluded volume are allowed to vary. To account for this, a method has been developed to calculate WAXS patterns using explicit atomic representation of water which has been implemented in the program called EXCESS[63]. As pointed out above, although WAXS patterns calculated with CRYSOL correspond well with experiments, this method of water representation (atomistic-water method) correctly captures the nature of solvation around proteins that previous methods might have missed[81].

Using molecular dynamics simulations and programs described above one can calculate scattering data to fit experimental WAXS data. Unfortunately, since protein coordinates for a protein cannot be calculated from scattering pattern, WAXS is mostly limited to proteins of known structure.

2.3.3 Time-resolved Wide Angle X-ray scattering

Time-resolved wide angle X-ray scattering (TR-WAXS) is a technique used to measure the nature and time-scale of global conformational changes and dynamics within proteins[82-88]. This method was initially developed at synchrotrons and hence the time resolution was limited to 100 ps due to the nature of the electron bunch duration within a ring. With the advent of XFEL's, the duration of the X-ray pulses is in the order of few tens of femtoseconds[89]. *Arnlund et al.,* show that TR-WAXS can be used to visualize protein dynamics in solution on multiphoton excitation of the photosynthetic reaction center of *B.viridis*[90]. In this study, the authors show that the backbone carbon atoms of the protein helices in RC_{vir} increase their internal distances on photon absorption which propagates from the interior of the protein and is rapidly distributed to the surrounding

solvent. This was the first experimental evidence to demonstrate that TR- WAXS is a powerful method to capture ultrafast structural motions that happen in the picosecond regime and possibly in faster time scales.

A similar experiment using TR-WAXS was performed on myoglobin where the authors demonstrated that, after photolysis of bound CO, Mb undergoes significant structural change in the picosecond timescale. The main observations in this study was that there was a rapid increase in the radius of gyration which occurred within 1 picosecond following which the protein undergoes damped oscillation with a ~3.6 ps timescale as the protein approached equilibrium[91].

One important point to note is that all the above studies were carried out with proteins that were triggered by light. In nature though only a tiny fraction of proteins are light sensitive and therefore it would be interesting to study the great majority of proteins which do not react to light. The work described in this thesis lays the foundation to trigger protein conformational changes using electric fields.

2.4 Coherent Imaging at an XFEL

In a conventional crystallography experiment, a single crystal is rotated through the X-ray beam and an image is taken in small increments, the angle of rotation can be user defined so that the entire reciprocal space can be sampled. In an SFX experiment, a stream of tiny crystals is passed through a highly focused X-ray beam and a diffraction image is collected whenever an X-ray pulse hits the crystal fast enough that it outruns the X-ray induced damage. Due to the peak brilliance coupled with the focused X-ray beam each crystal is destroyed on impact and therefore the conventional approach of using a single crystal does not work to sample the entire reciprocal space. The short duration of the XFEL pulses gives the opportunity to probe chemical reactions in the order of femtoseconds and hence termed Serial Femtosecond Crystallography.

The emergence of X-ray Free Electron Lasers (XFEL's) offers new possibilities to study biological filaments and the capability to perform single-particle imaging. The Coherent X-ray Imaging (CXI) beamline at the Linac Coherent Light Source (LCLS) was designed specifically for the high fluence intended to capture the full incident beam to

maximize the power density on samples of varying sizes[92]. Maximizing the number of photons incident on small targets is critical for imaging biomolecules and single particles. Previous studies at CXI have included a 32nm full- period resolution of a large mimivirus particle[93,94] and imaging individual live cells of cyanobacteria to nanometer resolution[95]. In an experiment conducted at the LCLS in October 2013 we performed one of the first fiber diffraction experiments at the LCLS for three different fiber systems (*Escherichia coli* pili, F actin and amyloid fibrils) **(PAPER IV)** which is further described in **Section 6.3** and another fiber system, microtubules **(PAPER V)** is also further described in **Section 6.5.**

Sample Delivery at a XFEL

Different methods have been used to deliver the samples into the path of the XFEL beam. One of the first among them was the Gas Dynamic Virtual Nozzle (GDVN) developed by De Ponte et al[96] at Arizona State University which is widely used for sample delivery.

Briefly, GDVN consists of a commercial hollow-core fused silica optical fiber as the inner capillary, as shown in Fig through which the sample is pumped through. The inner capillary is encapsulated by an outer glass capillary which helps to focus the outgoing liquid with helium gas to form a liquid jet. The sample could be either a solution or in the form of a crystal suspension. Sample delivery for structural biology studies with GDVN has been very successful at the LCLS, however in order to achieve a steady stream of liquid with uninterrupted interaction with X-rays and before Rayleigh break-up of the jet happens, the sample has to be pumped at rates typically in the order of 10 ms^{-1}. Such high flow rates are faster than the repetition rates of currently operating XFEL's and hence a majority of the sample is wasted without being probed[97]. GDVN was used as the sample delivery method for the experiments described in **PAPER IV** and **PAPER V**. Due to large consumption of protein sample it becomes prohibitive for scientists to purify complex proteins, especially proteins which require extensive optimization of purification and crystallization conditions, required by this mode of delivery.

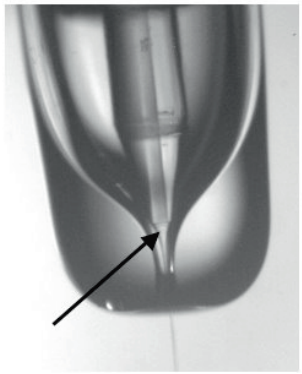

Figure 2.3: View of the exit end of the miniature version of gas dynamic virtual nozzle, photographed in operation with a water jet (arrow) emerging from the central capillary (360 µm OD, 50 µm ID, tapered outer wall) to be compressed by gas dynamic forces as the liquid stream passes with a co-flowing coaxial gas flow through the exit channel of the outer plenum (1.2 mm OD). A PTFE sleeve that centers the capillary within the outer housing is just out of view at the top of the photograph. (Adapted from DePonte et al., https://arxiv.org/abs/0803.4181)

Recent research has focused on designing a more efficient method of sample delivery and more importantly, a carrier medium which resembles the protein's natural environment. One approach to solve this problem is to use a lipidic cubic phase (LCP) jet for sample delivery. LCP is a liquid crystalline gel-like mesophase that mimics the native membrane like environment[98,99] and supports membrane protein crystallization including G-protein coupled receptors (GPCRs), microbial rhodopsins, ion channels, transporters, enzymes, photosynthetic complexes and β- barrel outer membrane proteins[100]. This viscous gel like lipid mixture produces a jet which can match the pulse rate (120 Hz at the LCLS) of the X-rays and thereby drastically reducing the flow rate and sample consumption.

CHAPTER 3

Effect of microwaves on the growth of microtubules

In PAPER I we provide a direct evidence for non-thermal effect of microwaves on the growth of microtubules using light-scattering at 365nm.

3.1 Design of the experiment

We designed a setup as shown in Figure 3.1 to monitor the polymerization of microtubules under the influence of applied microwaves and without the applied microwaves. All measurements with applied microwaves were performed at a frequency of 20 GHz. Tubulin polymerization was measured by recording the absorbance at 365 nm over time through a 1 mm quartz capillary. The entire set-up was enclosed in an acrylic-glass box (Figure 3.2) which could be temperature controlled by flowing hot-air into the system. The flow of hot air could be adjusted and was kept constant over a period of time so that the entire system was in equilibrium with the desired temperature. Another key aspect of this set-up was to measure the temperature of the solution in the capillary using a FLIR thermal camera while the measurement was being recorded. This enables us to observe the heating visually as well as providing a direct measurement of the temperature in the capillary.

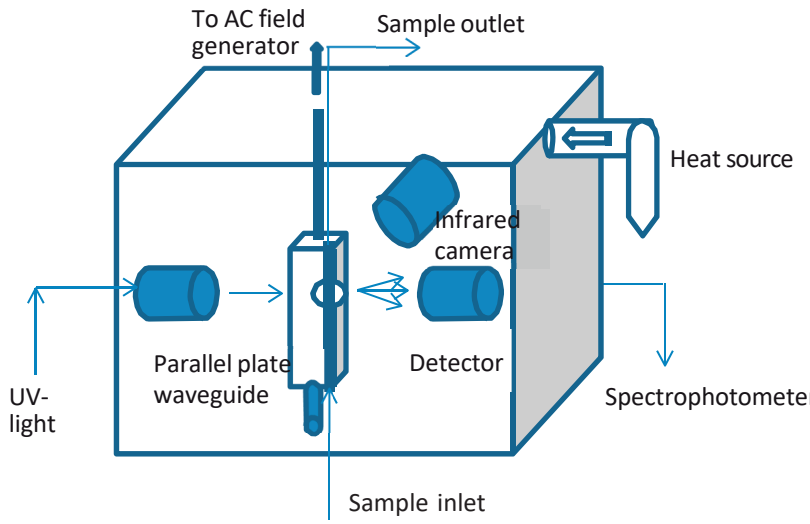

Figure 3.1: A simple schematic showing the setup for the light-scattering experiments

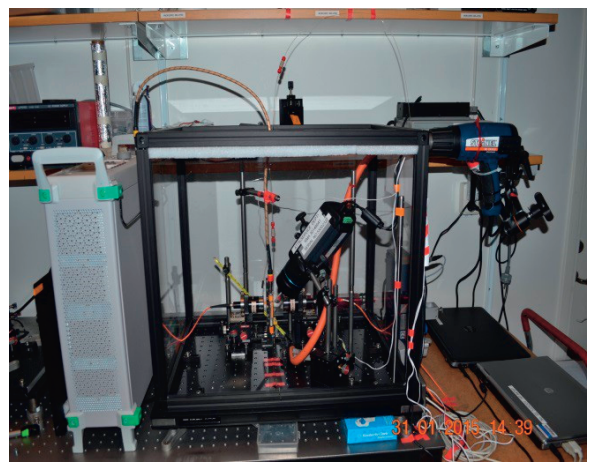

Figure 3.2: The set-up enclosed in an acrylic-glass box

Another important and vital component of the setup is the parallel-plate wave guide (Figure 3.3A) which is used to deliver microwaves onto a quartz capillary containing the tubulin sample. In figure 3.3B, you can see the heating of the solution when the AC field is on. A coaxial cable was used to transport the 20 GHz fields through the waveguide. The sample was pumped into the capillary at a flow rate of 10µl/min to avoid any formation of bubbles in the measurement region. The measurement began as soon as the sample reached the position in the

capillary.

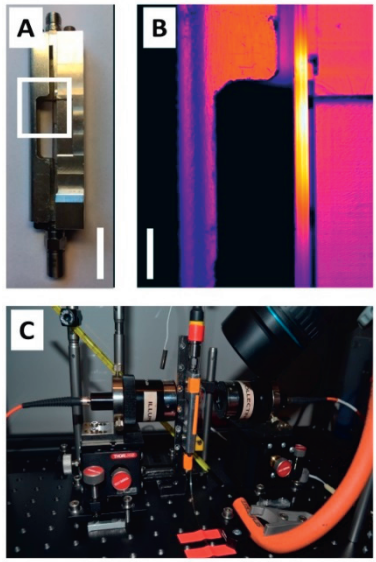

Figure 3.3: Experimental apparatus used to measure changes in optical density (O.D.) of microtubule samples during exposure to 20 GHz AC fields. **A**) Photograph of the waveguide used to deliver 20 GHz radiation onto a 1 mm diameter quartz capillary in which the sample was held. The white box indicates the region shown in the next panel. The white bar represents 2 cm. **B**) Infrared imaging of the sample within a quartz capillary during exposure to 20 GHz radiation. The region at which the sample is hottest (white) is the region from where the O.D. measurements were taken. The white bar represents 5 mm. **C**) Photograph of the microspectrophotometer used to record the O.D. at 365 nm with time during simultaneous exposure to microwaves. This entire setup was enclosed within a temperature controlled box. An infrared camera (FLIR thermographic) was used to monitor the temperature of the sample at the position at which its O.D. was recorded.

3.2 Sample preparation

The tubulin samples (10 mg/ml) containing GTP (2mM) were prepared on ice and loaded onto the sample position with a syringe pump. The tubulin samples were prepared from lyophilized bovine tubulin purchased from Cytoskeleton, Inc and were supplemented with either 0%, 5% or 10% glycerol and the final volume was made up to 100 µl with buffer.

3.3 Measurements of tubulin polymerization

The tubulin polymerization measurements were carried out under two conditions, with and without microwave fields applied. We performed three sets of measurements with the applied 20 GHz field using powers when no field applied, 18.2 dBM (66 mW) and 20.2 dBM (107 mW) and three different glycerol concentrations (0, 5 and 10% vol.) while simultaneously measuring the temperature with a FLIR thermal camera. Experiments without the application of field but only applying heat to the corresponding temperature of the applied field served as a control. So in total this corresponds to 27 measurement conditions. When 20 Ghz microwave fields were applied at intensities of 18.23 dBm or 20.3 dBm, the sample was heated by 4°C and 7°C respectively from the ambient temperature. Figure 3.4 shows the change in turbidity (O.D) of the sample when no field (blue), 18.23 (green) and 20.3 (red) 20 GHz fields are applied. After looking at the data visually and rejecting for bubbles and aggregates the remaining data was used for fitting.

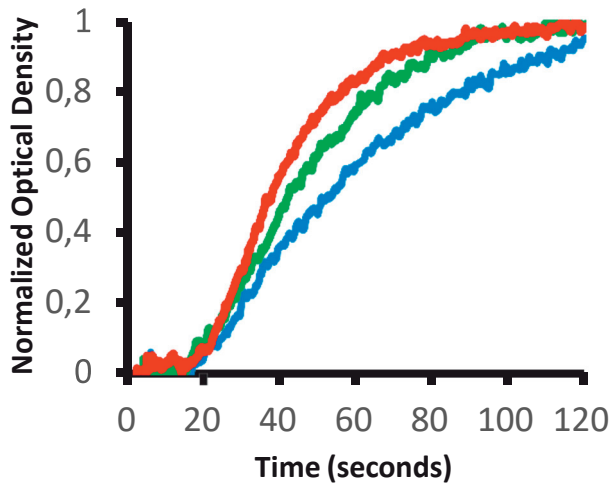

Figure 3.4: Measured changes in O.D. from samples of tubulin during the growth of microtubules and when a microwave field was applied. These data correspond to measurements performed on samples containing 5% glycerol, 10 mg/ml tubulin concentration, and with the temperature at the sample positon 33.5 ± 0.2 °C. These data are colored according to the applied 20 GHz microwave field strength as no field (blue), 18.2 dBm (green) and 20.3 dBm (red).

3.4 Data fitting and modelling

The polymerization of tubulin is reminiscent of sigmoidal kinetics characterized by distinct stages of nucleation, growth and saturation. The data collected from several measurements were offset so that the optical density at *t=0* was set to O.D = 0 and the endpoint optical density was normalized at O.D = 1 as shown in Figure 3.5. To this offset and normalized data we chose to derive a power law exponent by selecting a linear region on a log-log plot of O.D vs *t* between the range $0.15 \leq$ O.D. ≤ 0.5 which represents the elongation phase.

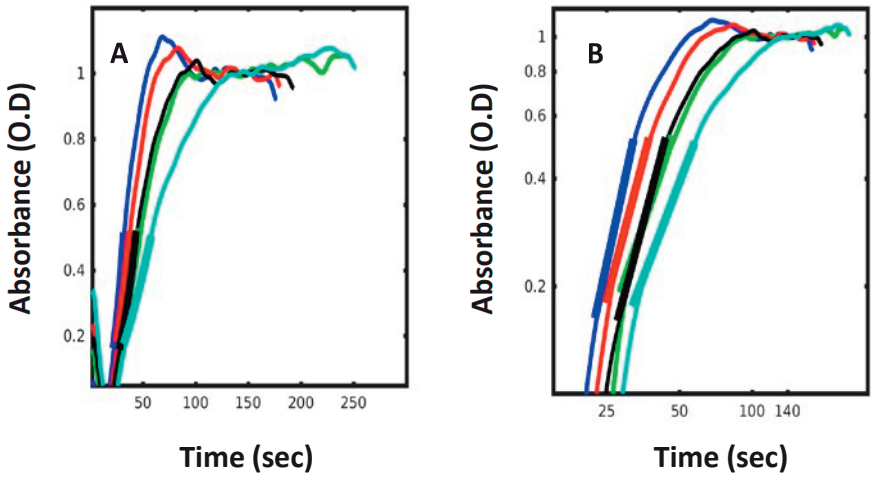

Figure 3.5: Plot showing the O.D *vrs* time dependance; (A) Plot showing the offset at t=0 and the normalization at O.D=1; (B) A log-log plot showing the fit region used to derive the power law exponent

To this region we then fit a power law using the equation;

$$O.D.(t)=A.(t/t_u)^b \qquad (3.1)$$

where A is a constant and b is the power law exponent and t_u is a single time unit which keeps the equation dimensionless on both sides. The t_{10}, time the O.D takes to reach 10% of its maximum value is also derived from this fitting. The data used in this analysis was grouped into three temperature domains (29-32°C, 32-35°C, 35- 37°C), three glycerol concentrations (0%, 5% and 10%) and three applied field strengths (No field, 18.2 dBm, 20.3 dBm). The power law exponent (*b*-values), Amplitude (*A*) and nucleation time (t_{10}) were extracted from these curves and based on the obtained *b*- values and t_{10} times, data which deviated more than 1.5 standard deviation were again visually inspected and rejected as outliers (18 curves of 163) when it was obvious that there were problems caused due to small bubbles within the sample which affected the scattering curves.

The growth of microtubules was modelled as a simple multi-step reaction with a forward and backward reaction for each step as described in the equation below[69]

$$d[MT_i]/dt = k^+_i [MT_{i-1}]\cdot[T_d] - k^+_{i+1} [MT_i]\cdot[T_d] + k^-_{i+1} [MT_{i+1}] - k^-_{i+1} [MT_i] \quad \text{.....(3.2)}$$

where $[MT_i]$ is the concentration of microtubules containing i tubulin dimers, $[T_d]$ is the concentration of the tubulin dimers, k^+_i is the rate of the forward additive reaction and k^-_i is the rate of the backward dissociative reaction. In this modelling, we assumed the forward (k^+_n) and backward(k^-_n) rate constant are equal for the nucleation (n) phase and an additional forward (k^+_g) rate constant and backward rate constant (k^-_g) to describe the growth (g) phase of a microtubule. The central idea behind this modelling is to see how different perturbations in the rate constant affect the t_{10} and b-values.

Figure 3.8B illustrates what happens when each of the four rate constant are varied. Scaling all four rate constants together strongly affects the rate of nucleation (t_{10}) whereas the power law exponent in the growth phase remains unperturbed (3.8B Orange circles respectively). On the other hand, if you vary the two rate constants corresponding to the growth phase; the forward rate constant (k^+_g) which is the rate at which the tubulin dimers are added (association) and backward rate constant (k^-_g) which is the rate at which the tubulin dimers fall-off (dissociation), the power law exponent (b-value) is strongly affected and only a small effect on the rate of nucleation ($t_{10\%}$) (3.8B Red and blue circle respectively). Varying the forward rate constants (k^+_n) and backward rate constant (k^-_n) of the nucleation phase leads to a b-value increase, as t_{10} decreases and k^+_n is increased which is in direct contrast for all three experimental observations. When k^-_n is varied it results in t_{10} being strongly affected than the b-value (3.8B Green and purple circles respectively).

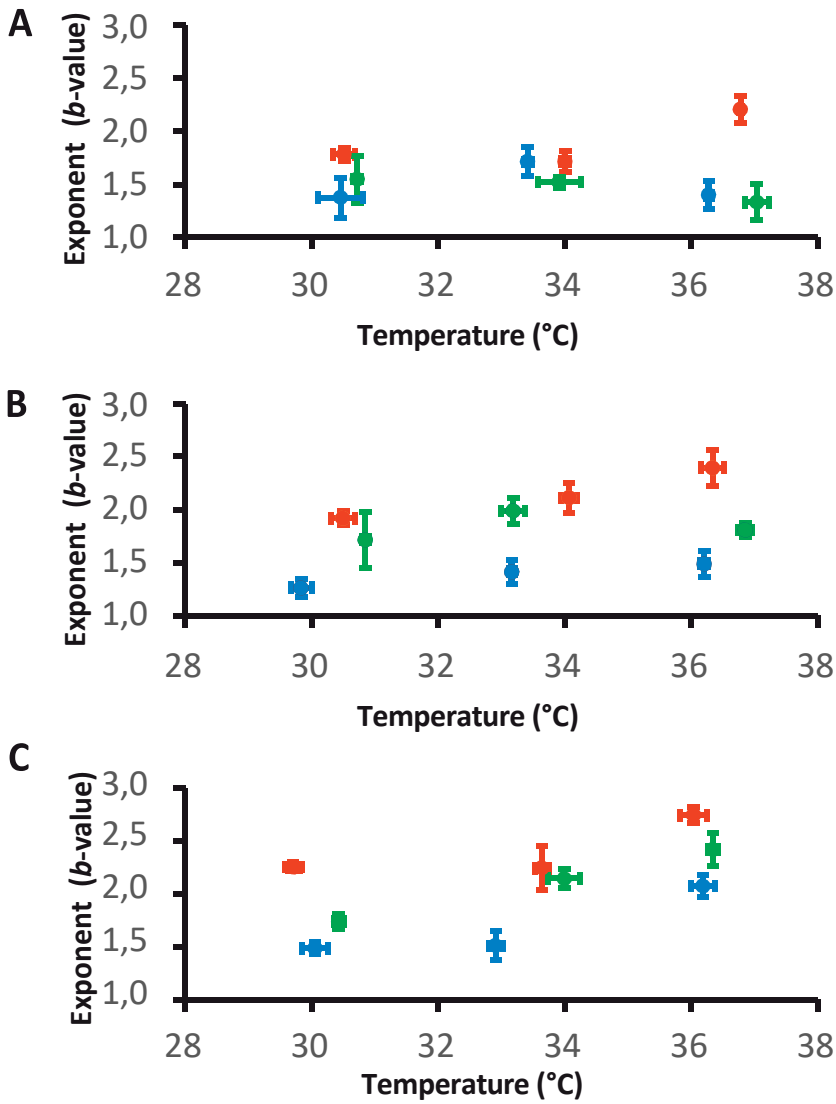

Figure 3.6: Summary of the influence of applied microwaves on the measured power-law (*b*-value) approximation. **A**, Plot showing the mean measurement of *b*-values resulting from fitting to Eq. 1 as a function of temperature for samples containing no glycerol. Error bars are calculated as s/√N, where s is the standard deviation of the set of measurements and N is the number of observations within the set. Data shown in blue were recorded without any applied 20 GHz field, whereas the field strength was 18.2 ± 0.2 dBm and 20.3 ± 0.2 dBm for data colored green and red respectively. **B**, Identical representation but for data recorded from samples containing 5 % glycerol. **C**, Identical representation but for data recorded from samples containing 10 % glycerol.

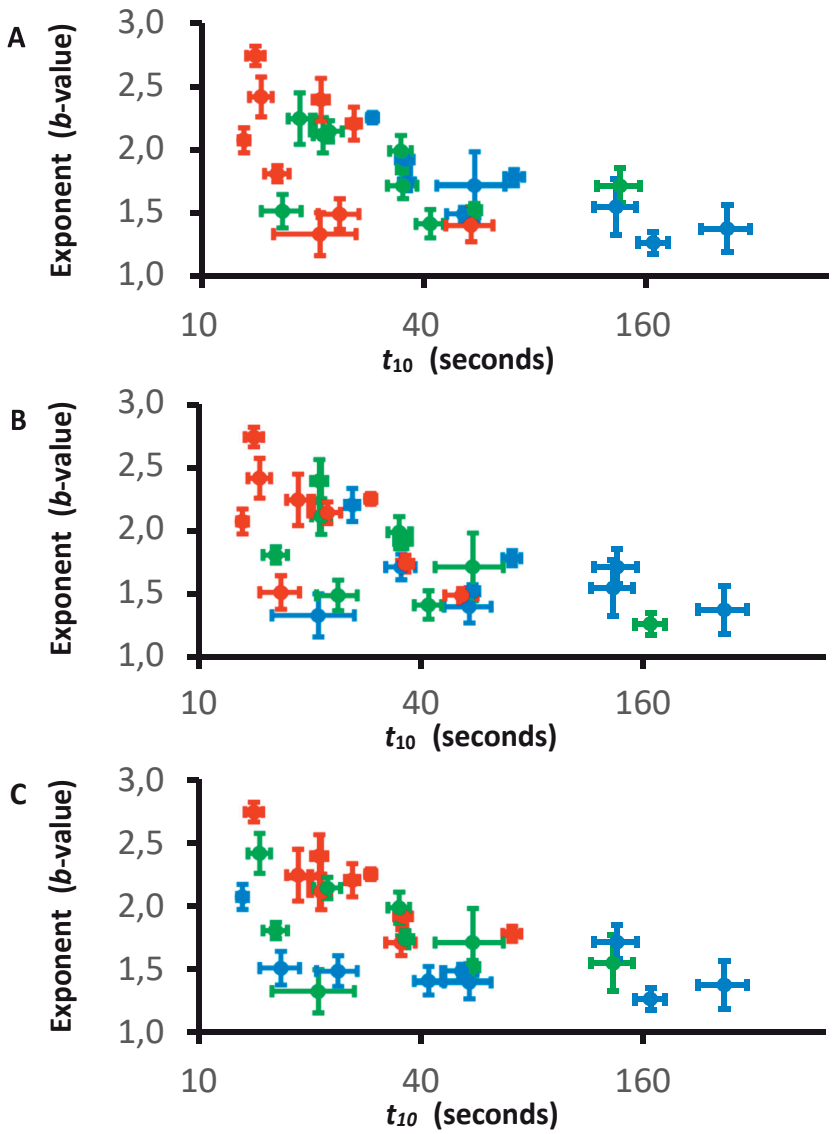

Figure 3.7: Influence of temperature, glycerol and microwave radiation on the growth of microtubules. Plots show the mean measurement of *b* and t_{10} values (with the time-axis plotted on a log scale) resulting from fitting to Eq. 1, with corresponding error bars, for all 27 sets of experimental observations. **A**, All 27 observations are colored with increasing temperature (blue, 30.2 ± 0.1 °C; Green, 33.5 ± 0.1 °C; Red, 36.4 ± 0.1 °C). **B**, All 27 observations are colored with increasing glycerol concentration (blue, 0 % glycerol; Green, 5 % ± 0.5 % glycerol; Red, 10 % ± 0.5 % glycerol). **C**, All 27 observations are colored with increasing applied 20 GHz field strength (blue, no field; Green, 18.2 ± 0.2 dBm; Red, 20.3 ± 0.2 dBm).

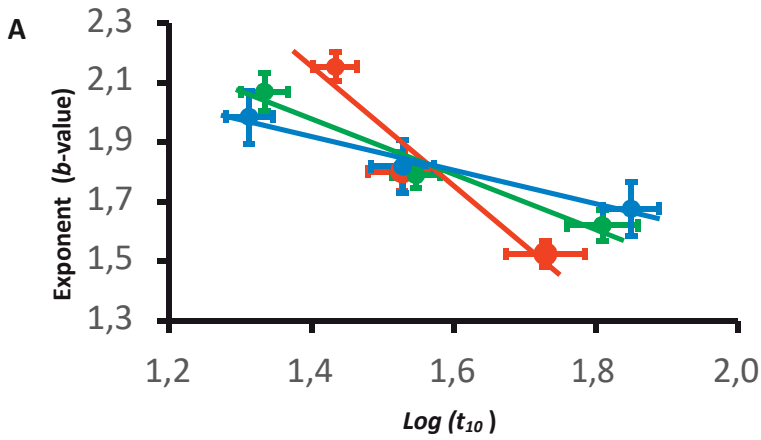
A
2,3
2,1
1,9
1,7
1,5
1,3
Exponent (b-value)
1,2
1,4
1,6
1,8
2,0
Log (t10)

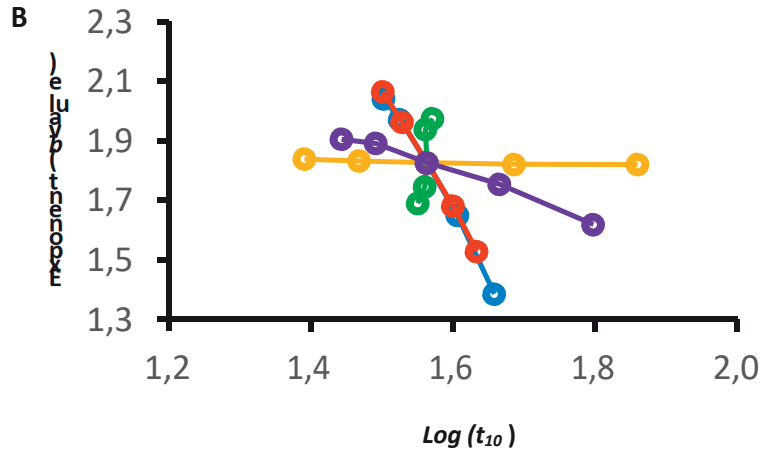
B
2,3
2,1
1,9
1,7
1,5
1,3
1,2
1,4
1,6
1,8
2,0
Log (t10)

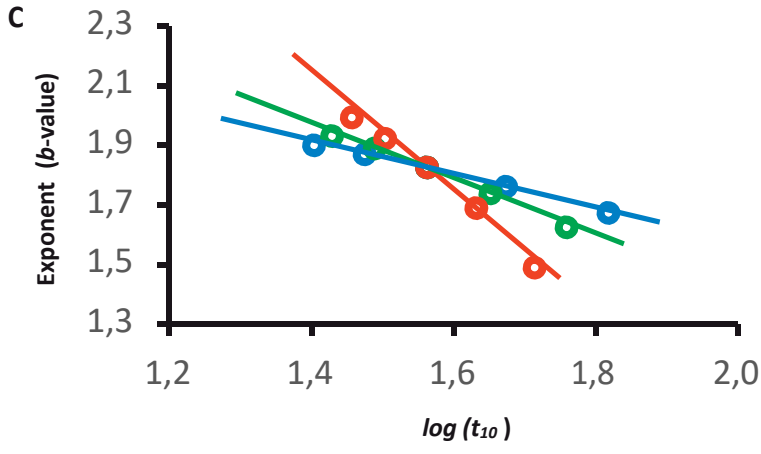
C
2,3
2,1
1,9
1,7
1,5
1,3
Exponent (b-value)
1,2
1,4
1,6
1,8
2,0
log (t10)

Figure 3.8: Modeling the influence of temperature, glycerol and microwave radiation on the growth of microtubules. **A**,The center-of-mass and error bars calculated from *b*-values and log(t_{10}) values for each of the sub-sets of data shown in Figure 3.7. Blue, the center of mass of each sub-set of data colored in Fig. 3.7A sorted according to temperature. Green, the center of mass of each sub-set of data colored in Fig. 3.7B sorted according to glycerol concentration. Red, the center of mass of each sub-set of data colored in Fig. 3.7C sorted according to applied 20 GHz field strength. **B**, The effect of changing the rate constants, k^{f}_{n}, k^{b}_{n}, k^{f}_{g} and k^{b}_{g}, that describe the nucleation (t_{10}) and elongation (*b*-values) phases of microtubule growth. Orange: the correlation between log (t_{10}) and *b*-values when all rate-constants are scaled together in discrete steps (increasing from right to left). This equates physically to rescaling the time parameter and therefore t_{10} values are strongly affected but (very minor) changes in *b*-values arise from numerical errors due to using discrete time steps. Blue: the correlation between log (t_{10}) and *b*-values as k^{f}_{g} is increased (decreased) in discrete steps (increasing from bottom to top). Green: the same correlation but with k^{f}_{n} is increased (decreased) in discrete steps (increasing from bottom to top). Red: the same correlation but with k^{b}_{g} is increased (decreased) in discrete steps (increasing from top to bottom). Purple: the same correlation but with k^{b}_{n} is increased (decreased) in discrete steps (increasing from left to right). **C**. Result of fitting a simple kinetics model describing microtubule polymerization to the linear correlation to the experimental data shown in **A**. Blue circles, the correlation between log(t_{10}) and *b*-values when fitting against the temperature dependent data; green circles, the same correlation when fitting against data recorded as the glycerol concentration is changed; red circles, the same correlation when fitting against data recorded as the applied microwave field is changed. Solid lines are the same data shown as solid lines in panel A.

3.5 20 GHz microwaves accelerate the growth of microtubules

Our results from the data fitting clearly show that the power law exponent (*b*-values) tend to increase under all conditions; increasing field conditions, increase in temperature and addition of glycerol. This is clearly illustrated in Figure 3.6 which shows the result of the power law fitting (*b*-values) to the data as a measure of the applied field strength (No field, 18.23 dBm and 20.3 dBm). Each of the three panels represent different glycerol concentrations (0% glycerol, 5% glycerol, 10% glycerol). This trend does not hold for lower temperatures and no glycerol since at these conditions the microtubules are not stable enough for growth to proceed which explains why there is no effect on applied electric field (Figure 3.6A).

Figure 3.7 illustrates all the 27 sets of data with each panel representing increasing temperature (Fig 3.7A, blue to green to red), increasing glycerol (Fig 3.7B, blue to green to red) and increasing field strength (Fig 3.7C, blue to green to red). A general trend is observed in all three plots with shorter t_{10} values and increasing *b*-values as the temperature, glycerol and applied field strength are increased. On closer inspection, one can clearly observe that this trend is more pronounced when the field strength is increased as compared to the increase in temperature with the influence of glycerol somewhere in the middle.

Figure 3.8 gives another representation by averaging the 27 sub-groups recorded at different temperatures (blue crosses), different glycerol concentrations (orange crosses) and different field strengths (red crosses). The change in the average time of nucleation (t_{10}) is represented from left to right and the change in the power law exponent (*b*-values) is represented vertically. While it is clearly visible that all three perturbations influence both the t_{10} and *b*-values, the most critical observation that can be made from these plots is that the temperature has a strong influence on t_{10} but less influence on the *b*-values. This is in contrast to that of the applied field strength where you see a strong influence on the power law exponent (*b*-values) as compared to the nucleation time (t_{10}).

This indicates that the applied field has much stronger effect on the growth of the microtubules as compared to the effect on the nucleation time.

3.6 Summary

From the results of the statistical analysis (*t*-tests (Table 1)), we can say with high confidence that the applied microwave field has a significant effect on the growth of the microtubule for all three *t*-tests (No field → 18.2 ± 0.2 dBm; 18.2 ± 0.2 dBm → 20.3 ± 0.2 dBm; No field → 20.3 ± 0.2 dBm) whereas the temperature has only pronounced effect on the rate of nucleation (t_{10}). While an increase in temperature (30.2 °C to 36.4 °C) also affects the *b*-values, the effect of lower temperatures on the power law dependence is not statistically significant. It is in agreement with the fact that raising temperature increases the reaction rate of most biological reactions and it is known that temperature increases the nucleation rate of microtubules[69]. Similarly, to temperature, increase in glycerol concentration (0 % to 5% and 5% to 10%) has more impact on the power law dependence but not on the increase from (0% to 5%).

From our simplified model to describe the microtubule growth kinetics (Eq. 3.2) and scaling all the four rate constants to variations in k^{+}_{g} or k^{-}_{g}, variables which strongly influence the microtubule elongation and growth we can reproduce the experimental correlations between t_{10} and *b*-values to a good approximation. Taken together, our results from both the experimental observations and modelling point towards the same conclusion; that perturbations induced due to changes in temperature, glycerol concentration and microwave field are the result of the influence on the forward and backward reactions in the elongationphase of a microtubule.

Table 1: *t*-test scores for comparison of t_{10} and *b*-values.

Comparison of b-values	**p-value**[†]
No field *vrs*.18.2 dBm	<0.0001
18.2 dBm *vrs.* 20. 3 dBm	<0.0001
No field *vrs.* 20.23dBm	<0.0001
30.2 °C *vrs.* 33.5 °C	0.498
33.5 °C *vrs.* 36.4 °C	0.092
30.2 °C *vrs.* 36.4 °C	0.012
0 % *vrs.* 5 % glycerol	0.120
5 % *vrs.* 10 % glycerol	0.007
0 % *vrs.* 10 % glycerol	<0.0001
Comparison of t_{10}-values	***p*-value**[†]
No field *vrs*.18.2 dBm	0.008
18.2 dBm *vrs.* 20. 3 dBm	0.551
No field *vrs.* 20.23dBm	0.001
30.2 °C *vrs.* 33.5 °C	0.004
33.5 °C *vrs.* 36.4 °C	0.002
30.2 °C *vrs.* 36.4 °C	<0.0001
0 % *vrs.* 5 % glycerol	0.004
5 % *vrs.* 10 % glycerol	0.080
0 % *vrs.* 10 % glycerol	<0.0001
[†]Considered significant if $p \leq 0.05$	

CHAPTER 4

Adapting a crystallography beamline to perform difference WAXS studies

In Paper V we adapted a crystallography beamline at MAX-II synchrotron in Lund to perform and validate solution scattering experiments. The experimental results obtained here could be used to prove initial proof-of-principle concepts without the requirement of highly specialized beamlines and further expanded in scope to perform time resolved WAXS experiments at other synchrotron and XFEL sources.

4.1 Beamline environment

The beamline I911-2 is a part of the MAX II storage ring based on superconducting wiggler[101,102], where two beamlines (I911-2 and I911-3) are operated for macromolecular crystallography. The I911-2 beamline which was used in this study is a fixed wavelength beamline (1.04 Å) equipped with a Mar165 CCD detector and a photon flux of 10^{11} photons/sec. We adapted this beamline to perform steady state wide angle solution scattering experiments by combining several approaches.

First we designed a flight tube (helium cone) to fit into the dimensions of the detector (Figure 4.1A). A flight tube filled with helium is critical to perform solution scattering experiments to reduce the beam scattering from air and enhance data quality. While enclosing the detector in vacuum is a better option[103,104] it is expensive and time consuming to build one. The practical option for our experimental needs was to use helium which is a good alternative to vacuum and time resolved solution scattering experiments have been performed in earlier studies using helium as a medium[88]. Another crucial aspect of solution scattering is

that the difference scattering could be very small and hence it is imperative to reduce the background scattering from other sources. The center of the helium cone had a beam stop to prevent the direct X-ray beam hitting the detector which can be manually controlled externally.

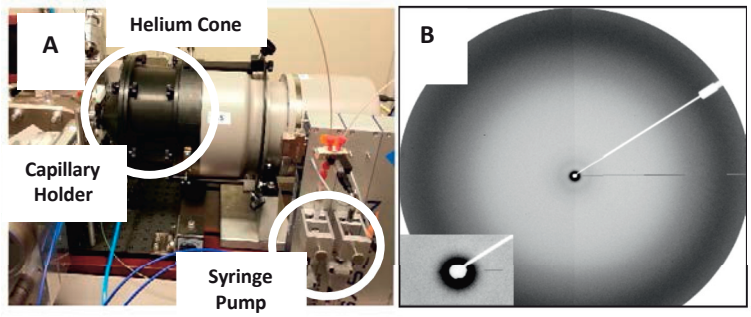

Figure 4.1: Difference WAXS setup built on the protein crystallography beamline I911-2 of MaxLab. **A** Photograph of the setup on the beamlines used during these experiments. The helium cone, sample holder and pumps are indicated. **B** X-ray scattering from protein samples when the cone is filled with helium and a 0.5 mm diameter beamstop is well aligned.

We used a neMESYS syringe pump to continuously pump the protein solution so as to minimize the radiation damage between successive X-ray shots. The syringes with sample are connected with tubing to a quartz capillary where the X-rays interact with the protein sample. The position of the capillary with respect to the X-rays can be precisely controlled with a motorized XYZ stage.

4.2 Experiments to validate the setup

We performed WAXS experiments on two different protein systems to check if our setup is sensitive to structural changes in the WAXS region.

4.2.1 Phytochromes

In our first study we used bacteriophytochromes from *Deinococcus radioduran* to see if we can capture light induced structural changes. Briefly, phytochromes can interconvert between two states Pr and Pfr when illuminated with light of two different wavelengths. To trigger the conformational changes two LED sources, operating at 780 nm and 660 nm were used to switch the samples between two states Pfr → Pr and Pr → Pfr, respectively. After rejecting for outliers, we

then calculated the difference scattering between the two LED exposures[87,105]and compared with the difference scattering collected earlier by Takala et al.,[87] at the CSAXS beamline at the Swiss Light source as seen in Figure 4.2**.** Figure 4.2A shows the difference signal (in red) between the two states recorded at MaxLab and the associated heating signature due to illumination (in blue). Phytochromes served as an excellent test system due to the large difference signal observed when the monomers move apart by ~3 nm during the Pr → Pfr transition[87]. As seen in Figure 4.2 a large oscillating difference signal was very apparent at low angles (0.1 $Å^{-1}$ ≤ q ≤ 0.2 $Å^{-1}$) in the data collected at Maxlab and matched with data collected previously at another synchrotron (SLS).

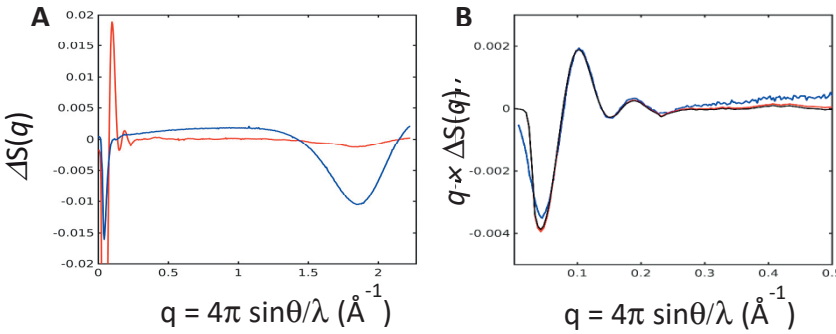

Figure 4.2: A) Difference WAXS scattering signal recovered from phytochromes (red line): DS(q) = S(q)^{Pfr} – S(q)^{Pr}, after samples were illuminated with 780 nm or 660 nm light, respectively. The difference WAXS scattering recovered due to heating (blue line): DS(q) = S(q)^{IR} – S(q)^{dark}, where IR light of 1470 nm was used to heat the samples without initiating the light-driven conformational change. **B**) Difference WAXS signal q×DS(q) showing data recorded from phytochromes before (red) and after (black) the influence of heating was removed from the signal. For comparison, similar data but recorded at the cSAXS beamline of the SLS is shown (blue).

4.2.2 Spinach aquaporin

For our next experiment we recorded solution scattering data for a non-photoactivated protein, wild-type spinach aquaporin (SoPIP2;1). For SoPIP2;1, a membrane protein which regulates water transport across the plant membrane we used photoactive calcium Ca^{2+} as a means to trigger the structural changes in SoPIP2;1[106,107]. Although SoPIP2;1 itself is not activated by light, the Ca^{2+} which acts as a trigger has to be released from its caged form with UV light for it to become active in solution[108,109].

To initiate the Ca^{2+} triggered activation of SoPIP2;1, we used UV light at 365nm to release the caged Ca^{2+} into solution. We used a pulsed IR laser at 1470 nm to match the heating caused by the illumination of UV-light on the sample.

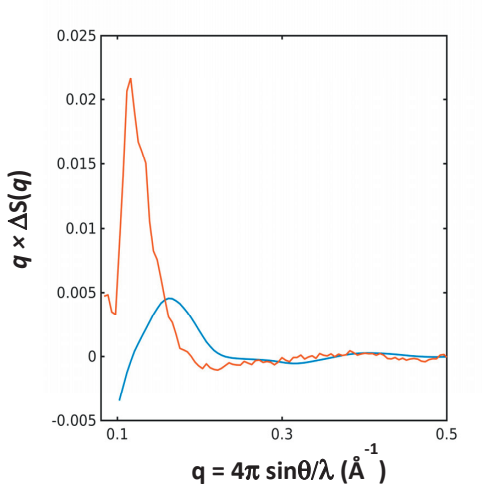

Figure 4.3: Difference WAXS changes in SoPIP2;1 associated with the release of caged Ca^{2+}**.** The experimental data $q \times DS(q)$ where $DS(q) = S(q)^{UV} - S(q)^{dark}$ is shown in red, where UV light of 365 nm was used to release the cage. A prediction (blue line) based upon known crystallographic structures of the open and closed forms of SoPIP2;1 is shown for comparison.

The experimental difference signal (Figure 4.3) shows some distinct features in the low q region ($0.1\ Å^{-1} \leq q \leq 0.2\ Å^{-1}$) and additional oscillations at higher q ($0.2\ Å^{-1} \leq q \leq 0.6\ Å^{-1}$). As can be seen in the Figure 4.3 the fit is not perfect probably due to the model using a lipid bilayer instead of a detergent micelle and an incomplete model to

the open confirmation. Additionally, the flexible N- and C-termini are not included in the model at present and the fit is expected to improve if they are included. The difference signal obtained from the conformational changes in SoPIP2;1, again demonstrates the sensitivity of this beamline to structural differences in non-light activated proteins

4.3 Summary

In **PAPER II** we have demonstrated using two protein systems that the I911-2 beamline can be used to perform solution scattering experiments with good reliability. Similar experiments can be performed at other synchrotrons in underutilized beamlines to establish a proof-of-principle concept which will enable to perform time-resolved solution scattering experiments in other dedicated beamlines.

Chapter 5

Microwave induced structural perturbations in microtubules using solution X-ray scattering

In Paper III, the idea was to expand the light scattering studies on the influence of microwaves on the microtubule growth dynamics to X-ray scattering studies of the influence of microwaves on the structure. In Chapter 3 we showed that 20 GHz microwaves accelerate the growth (elongation phase) of the microtubules. In this study we use SAXS and WAXS to probe for structural changes in microtubules on exposure to 20 GHz microwaves at the cSAXS beamline of the Swiss Light Source (SLS).

5.1 Sample preparation

Tubulin samples were pre-polymerized at a concentration of 285 μM (corresponding to 32 mg/ml) in the presence of 2 mM GTP and 10.6 % glycerol. The samples were held in a water bath at 37°C for ~20 min to form microtubules. Once polymerized samples were kept at 37°C in an Eppendorf Thermostat inside the experimental hutch. The sample solution was then pumped at a constant flow of 0.2 μls^{-1} through the capillary and the X-ray beam position. This enabled the sample to be constantly replenished. The tubulin samples exposed to X-rays were discarded.

5.2 Exposure of microtubules to microwaves

The sample was transported through a parallel-plate waveguide based flow-cell system which was used for light scattering studies in Chapter 1**.** The sample was flown through a 1 mm quartz capillary held in between the two waveguide plates and a coaxial cable fed the 20 GHz fields from a signal generator through the waveguide. The signal generator was controlled with a TTL pulse and synchronized with the detector shutter signal. The TTL signal initiated a pre-programmed routine on the microwave device.

5.3 Experimental set-up and data collection

During this experiment we collected both SAXS and the WAXS data for microtubules with a Pilatus 2M detector and a Pilatus 300K detector respectively. Both the SAXS and the WAXS detectors were enclosed in a vacuum tube. By using this combination of both the SAXS and WAXS detectors we were able to record the strong scattering of microtubules in the $q \leq 0.1$ Å^{-1} while also simultaneously recording the heating of the sample on the WAXS detector at $q \geq 1.0$ Å^{-1}. The Pilatus detectors operated at an acquisition rate of 20 Hz with 50 ms X-ray exposure for each frame and 3 ms readout time.

In this experiment we used two different exposure protocols (Figure 5.1). For the first protocol (slow switching), we exposed the sample to the microwaves (ON) continuously for 20 seconds (400 X-ray frames) followed by 30 second (600 X-ray frames) cool- down period (OFF) with no microwaves. In the second protocol (fast switching) we alternated the microwaves between ON/OFF with a 500 ms exposure (10 X-ray frames ON) followed by 500 ms of no microwaves (10 X-ray frames OFF). This was then followed by a 6 second cool-down period with no microwave exposure. The switching protocol does not allow us to turn off the signal generator completely and hence we used -20dBm corresponding to 10 µW which we consider as OFF in these experiments.

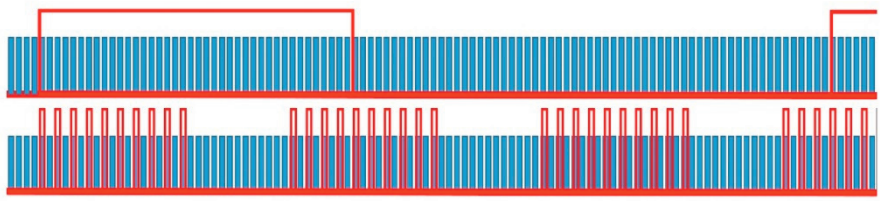

Figure 5.1: Difference X-ray scattering studies of microtubules. Schematic of the two experimental protocols used in this study. Data were recorded in both experiments using X-ray exposures of 50 ms. Blue rectangles represent ten frames summing to 500 ms of X-ray exposure. Protocol 1 recorded X-ray scattering data during 20 sec of microwave illumination (red rectangle, ON) followed by 30 sec without microwave radiation (OFF). Protocol 2 alternated between 500 ms microwave exposure (ON) and no microwave radiation (OFF) for 10 sec, followed by 6 sec during which the sample equilibrated with ambient temperature.

5.4 Interpretation of difference curves

We recorded difference scattering data ($\Delta S(q) = S(q)^{ON} - S(q)^{OFF}$) for both protocols (Figure 5.2). For protocol 1, the temporal dependence of the heating and cooling cycles results in the temperature of the ON samples being warmer than the OFF samples which is visualized by the positive peaks $\Delta S(q)$ around q = 1.4 Å^{-1} and 2.4 Å^{-1} and the trough centered on q = 1.9 Å^{-1} (Figure 5.2). A key difference to be noted here is that the pattern of peaks and troughs in the WAXS region for the Protocol 2 is opposite to that of Protocol 1. Thus the average temperature is a fraction of degrees warmer for the OFF when compared to the ON. SVD analysis of WAXS data gives us an understanding of the increases and decreases in temperature across the data-collection cycle and is in good agreement with measurements taken with an infrared camera to characterize the temperature change (Figure 5.3A). For Protocol 2, you could see a jagged edge associated with the ON/OFF cycles during the first 10 seconds when the sample is heated followed by the 6 second cooling down period (Figure 5.3B). This provides an explanation as to why the average temperature during the first 10 seconds in Protocol 2 was higher during the OFF cycle when compared to the average temperature during the ON cycle.

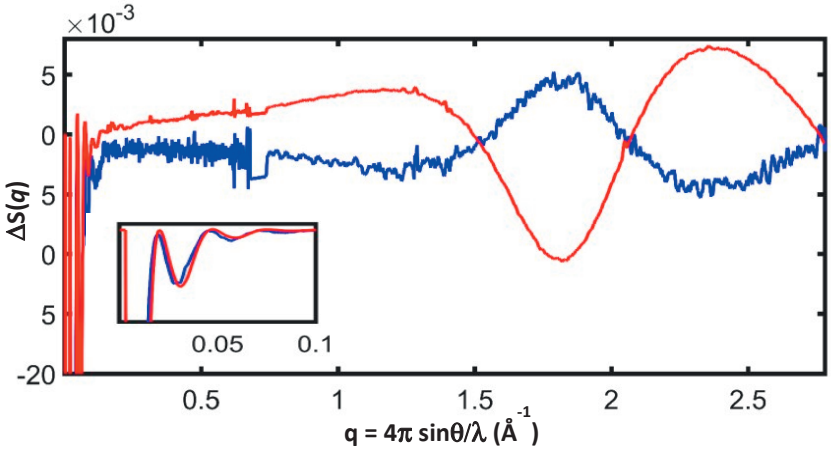

Figure 5.2: Experimental changes in the X-ray scattering using the two protocols. Protocol 1 (red line) caused changes in the WAXS region with positive peaks visible around q = 1.4 Å^{-1} and 2.4 Å^{-1} and a trough at q = 1.9 Å^{-1} that are characteristic signals for sample heating. Data recorded using Protocol 2 (blue line) showed that similar features are visible but with the opposite sign (representing net cooling). The inset shows that the difference scattering in the SAXS region. Difference data recorded using Protocol 2 are scaled 25 fold (scaled tenfold for the inset) to match the difference scattering recorded at low angle using Protocol 1.

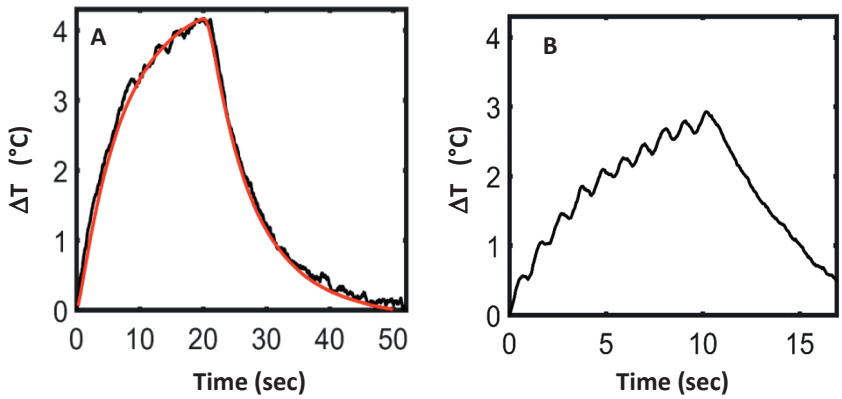

Figure 5.3: A) Amplitude of the principal component following singular value decomposition (SVD) of the difference scattering curves in the WAXS region when using Protocol 1 (black line). For comparison the temporal evolution of the sample heating recorded using an infrared camera is shown (red line). **B)** SVD analysis of heating when using Protocol 2. The jagged nature of the rising edge in this curve is due to the 2Hz ON/OFF cycles during the first 10 sec.

Another interesting observation is that, in the WAXS region despite having similar features but with opposite sign when comparing Protocol 1 and Protocol 2, the difference $\Delta S(q)$ in the SAXS region show very similar difference features but with the same sign. This is a clear indication that the difference signal seen in the low-q region is not due to temperature since the SAXS region would also have shown opposite difference curves.

Taking into account the differences in amplitude of the difference scattering between Protocol 1 and Protocol 2, Protocol 1 produces ten times larger than that from Protocol 2. This could be due to two possible scenarios. The first could be due to the induced effect takes some time to build up and due to which the population of microtubules that are affected will continue to grow during the 20 second microwave exposure. The other scenario could be that the induced effect could take time to reverse which could lead to a larger fraction of perturbed microtubules still remaining in the OFF position leading to a smaller amplitude when compared to Protocol 1. Both the scenarios can be considered as plausible since the additional 500 ms exposure in Protocol 2 is $1/40^{th}$ of the 20 second exposure used in Protocol 1.

By looking at Figure 5.4 we can see that the trends in the total scattering recovered from Protocol 1 (peaks and troughs) have a strong correspondence with the location of the peaks from the predicted scattering of microtubules. A basic interpretation would suggest that 4% of the microtubules simply dissolved on exposure to X-rays, although it ignores the fact that dissolving microtubules will increase in free tubulin subunits and hence an increase in overall X-ray scattering

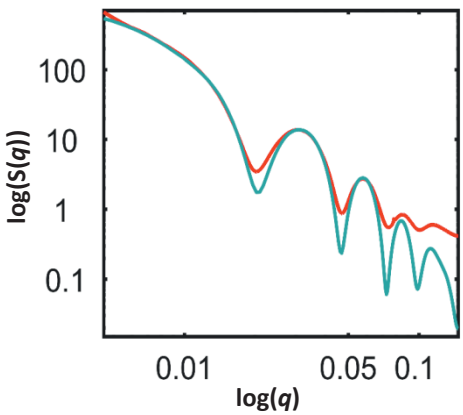

Figure 5.4: Experimental scattering curves (red line) recorded from microtubules after integrating the X-ray scattering images in concentric rings. Theoretical predictions for the X-ray scattering from an extended 14 pf microtubule (grey line) shows good agreement with these experimental data.

Another interpretation regarding the effect of microwaves on microtubules could be real structural effects consistent with measured X-ray scattering differences. Two possibilities of conformational disorder have been explored as shown in Figure 5.5, assuming that the microtubule becomes expanded (orange line) or the microtubule becomes elongated (green line) as illustrated in Figure 5.6. Theoretical predictions for $\Delta S(q)$ associated with the expansion of the diameter do not provide a good match with the experimental data but the prediction associated with the elongation of a microtubule provide a good match with the experimental data for q ≤ 0.1 $Å^{-1}$. Additionally, we provide a difference curve between microtubules and dimers as measured during the experiment (black line). However, more data is needed to find out the structural perturbations behind these difference curves.

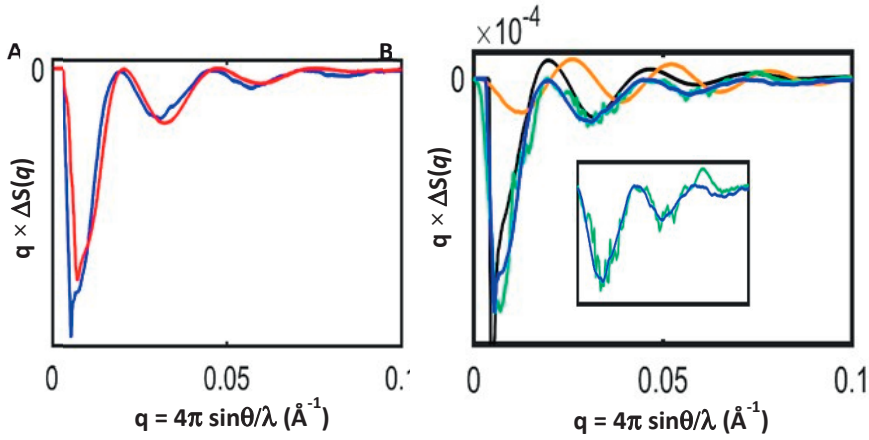

Figure 5.5: Changes in the X-ray scattering from microtubules upon exposure to 20 GHz radiation. **A**) Changes in the X-ray scattering, DS(q) = S(q)^{ON} – S(q)^{OFF}, resulting from Protocol 1 (red line) and Protocol 2 (blue line). Difference data recovered using Protocol 2 are scaled tenfold for comparison with data recorded using Protocol 1. **B**) Comparison of the experimental differences DS(q) recovered using Protocol 2 (blue line) with predictions assuming different models. Orange line, theoretical prediction when a 14 pf microtubule is assumed to expand by 0.1 %. Green line, theoretical prediction when a 14 pf microtubule is assumed to be elongated by 0.12 %. In this model elongation is achieved by the spacing between αβ-tubulin dimers being increased, rather than the structure of αβ-tubulin being distorted. Black line, experimental difference curve when the ratio of free tubulin to microtubules is shifted to mimic the effect of microtubules dissolving.

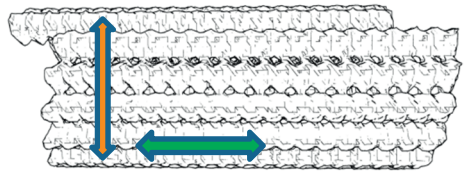

Figure 5.6: Structural model of a microtubule illustrating the nature of the structural perturbation examined in 5.5B. Orange double arrow, the spacing between tubulin dimers is expanded to create a microtubule model having a larger diameter; Green double arrow, the spacing between tubulin dimers is expanded to create an elongated microtubule model.

5.5 Summary

In this work we have used microwaves to induce structural perturbations in microtubules while simultaneously recording SAXS and WAXS data. We demonstrate that we can obtain reproducible difference curves which hints at some sort of conformational change happening in the microtubule. Based on initial theoretical predictions we hypothesize that microwaves could trigger the elongation of microtubules as visualized in the low-*q* region $q \leq 0.1$ Å^{-1}.

CHAPTER 6

Coherent Diffractive Imaging of fibers and filaments at an XFEL

In **Paper IV** and **Paper V** we performed coherent imaging using XFEL radiation on several filament systems such as microtubules (Paper V) and *Escherichia coli* pili, F-actin, amyloid fibrils and gelsolin amyloids (Paper IV). The goal was to obtain single-shot fiber diffraction patterns while also demonstrating the flow alignment of five different biological systems in a liquid micro-jet also known as GDVN (Gas Dynamic Virtual Nozzle).

XFEL- based science has taken off rapidly with great strides made in obtaining protein structures and intermediate reactions previously inaccessible, due to the high time-resolution achievable with XFEL pulses. One of the important goals of XFEL radiation is to study biological molecules without the need for crystals. Fiber diffraction has been used to study biological filaments since the early 1920's when Michael Polanyi used X-ray diffraction to study cellulose and formulated the theoretical concept for fiber diffraction[110,111].The most famous demonstration of X-ray fiber diffraction was the determination of the double helical structure of DNA[112-114].

6.1 Basis of fiber diffraction

Fiber diffraction takes advantage of the one-dimensional translational symmetry of the filaments and consequently the diffraction intensity is between 3D crystals and single molecules. As the sample is rotated around the fiber axis, the X-ray diffraction pattern remains unchanged. An intrinsic feature of the polymers is that they repeat periodically along their lengths and so the scattering lines are confined to the layer lines of the helical polymers[115]. However, the alignment of fibers happens only in rare cases. To circumvent this problem several techniques have been employed to generate the alignment of fibers to get high quality diffraction patterns. One such method was to use oriented polycrystalline samples which are flexible *in vivo* to perform fiber diffraction[116]. Fiber diffraction largely

depends on the orientation of the sample and hence some extreme measures such as having protein concentrations as high as 100 mg/ml have been used to generate flow orientation in a glass capillary. There are several other factors which could influence the orientation such as the length of the filament, ionic conditions, pH and application of magnetic fields[117,118].

6.2 Flow alignment of fibers and filaments in a GDVN

In experiments performed at the LCLS in October 2013, we used flow alignment through a gas dynamic virtual nozzle (GDVN). In PAPER IV and PAPER V we used GDVN to flow align different samples.

In PAPER IV all the samples described above were prepared as sols. A sol can be described as a colloidal solution containing a suspension of small particles, in this case biological filaments, which are delivered in a continuous liquid medium. In order to achieve single shot fiber diffraction, oriented filaments prepared in sols becomes necessary. To overcome this limitation, we employed a GDVN to deliver the samples into the path of the X- FEL beam. In previous studies by Popp et al., a large amount of protein (>1 g) has been used to optimize the process of filament orientation[119]. In a GDVN (Figure 6.1 & 6.2), helium gas flows co-axially acting as a virtual nozzle focusing the liquid jet and when one accelerates the flow of the fluid, the cross-section of the liquid jet is reduced. The extended filaments flow-align due to the differential flow speeds in the virtual nozzle.

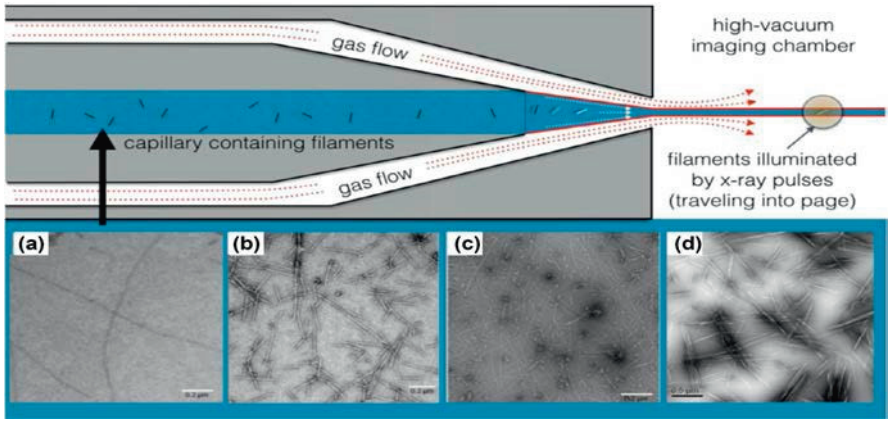

Figure 6.1: Flow alignment of filamentous samples in the GDVN. Top: Schematic of the GDVN, where a suspension of filamentous samples inside a capillary is focused into a micro-jet in the high-vacuum X-ray imaging chamber using a virtual nozzle formed by a co-axial gas flow. Bottom: Filament systems used in these studies. (a) Electron micrograph of F-actin filaments formed by polymerizing G-actin with 50 mM KCl for 2 hr in the presence of gelsolin (4,000:1).(b) Electron micrograph of type I pili that were sheared from the surface of E. coli. (c) Electron micrograph of AgelN amyloid fibrils formed in water after 5 days of incubation. (d) Electron micrograph showing the needle-like appearance of the G11A aggregates.

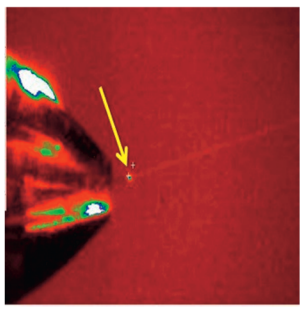

Figure 6.2: Microjet (left) and the stream of filamentous particles (fine red line) intersected by the XFEL beam at the arrow

6.3 Fiber diffraction of Actin, *E.coli* pili, amyloid fibrils and G11A synuclein

Four different filament systems were studied to study the structure of biological filaments with an XFEL. All these samples were flown through a GDVN (Figure 6.1) resulting in a micro-jet which were subsequently intercepted by the XFEL beam. Various aspects of the micro-jet had to be controlled precisely so that the XFEL beam interacts with a continuous stream of liquid.

With a future goal to achieve single particle imaging, the jet diameter was controlled by the nozzle size, pressure of the liquid in the nozzle and the rate of the gas flow around the nozzle. It is also important to reduce the scatter from the jet solvent to vacuum interface and therefor the jet diameter (4-5 µm) was chosen to be larger when compared with the X-ray diameter (0.2 or 1 µm). The collimation of the liquid jet in a GDVN happens primarily due to viscous shear forces from the gas (helium) flow acting on the sample-laden liquid jet. This focusing or collimation causes the filaments or the proteins in solution to experience extensional stresses which forces the initially randomly oriented molecules to realign along the central axis of the flow. Additionally, due to the shear forces exerted on the liquid exiting at the nozzle by the flowing gas, the flow of the liquid will be faster than at the central axis. Hence, the filaments in such a flow profile will be extended and experience a torque resulting in flow alignment.

6.3.1 Data collection and sorting

Single-shot diffraction images of the different filament samples were collected with a CSPAD detector at 120 frames per second. The images obtained by this mode were computationally classified to select for filaments that were more clearly aligned. This method also allowed to minimize the overall disorientation of the fiber diffraction patterns. The diffraction patterns with clear alignment were identified by simply looking at the patterns and sorting with a method called angular-resolved intensities binning.

For actin we obtained diffraction patterns containing aligned filaments with weak background (Figure 6.3a) were classified as small clusters and subsequently averaged to produce a diffraction pattern as shown in figure 6.3b**.** These averaged patterns gave rise to layer lines at 5.96 nm and 5.1 nm, reflections typical of actin filaments corresponding to the

right and left handed helices[120]. The emergence of these layer lines is also proof that the actin filaments remained intact in the microjet within the vacuum chamber. The alignment and the subsequent averaging enabled us to estimate the disorientation SD to 5 degrees.

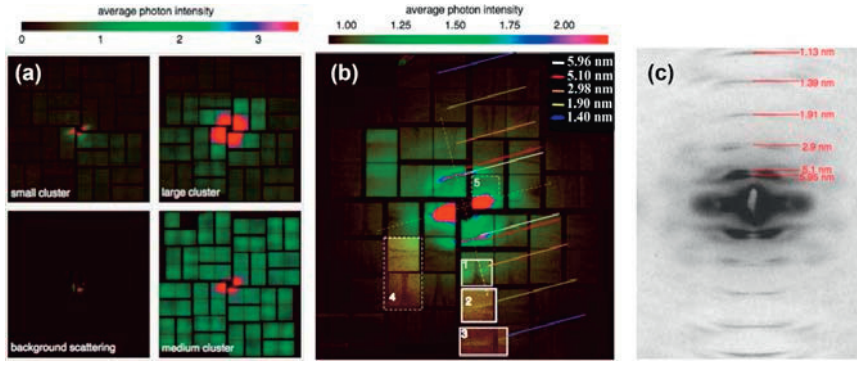

Figure 6.3: XFEL fiber diffraction from actin filaments colored according to photon intensity per detector pixel. (a) A total of 52,738 patterns were collected and 26,610 were classified as usable (small or medium cluster of aligned filaments), the remainder containing large, non-oriented clusters of filaments or strong background scattering. (b) An averaged XFEL fiber diffraction from the selected images that shows the most prominent layer lines. The 5.96 nm (order l56) and 5.1 nm (order l57) layer lines are clearly visible, which arise from the protomer spacing in the right and left handed long and short pitches of the actin helix, respectively. (boxes 1–3) Weaker, higher-order layer lines are also labeled and enhanced for contrast (e.g. 2.98 nm (order l513) layer line, which arises from the separation of the long pitch actin strands) and (box 4) shows detector artifacts. (c) Qualitative comparison against features from a fiber diffraction pattern collected from capillary aligned F-actin on a rotating anode X-ray generator.

E.coli pili (type 1 pili) showed prominent features visible at approximately 2.4 nm and 1.16 nm layer lines along with an equatorial line at 4.2 nm from the obtained diffraction images (Figure 6.4a) as well as the averaged patterns (Figure 6.4b). These prominent features represent the helical repeat, the second order of the helical repeat and the helical radius. Comparison of the XFEL averaged fiber patterns (Figure 6.4b) with patterns obtained from synchrotrons (Figure 6.4c) show similarity between the two techniques and the alignment of fibers was similar to synchrotron obtained patterns.

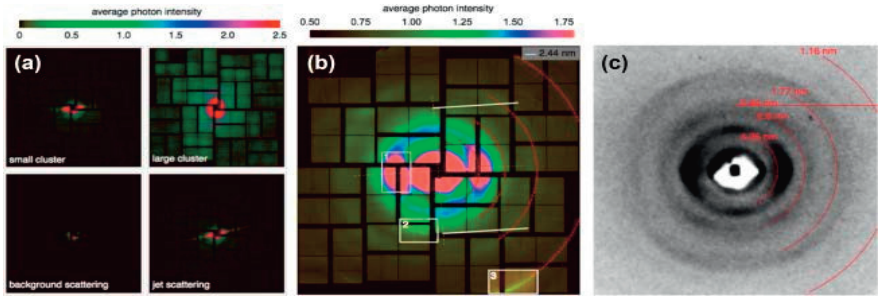

Figure 6.4: XFEL fiber diffraction from *E. coli* type 1 pili colored according to photon intensity per detector pixel. (a) 81,352 such patterns were either classified as usable (containing a small cluster of aligned filaments) or unusable (large non-oriented clusters of filaments; strong scattering from edges of micro-jet; strong background scattering). Only the most intense, usable patterns were selected and averaged. (b) An averaged XFEL fiber diffraction from 11,244 images that shows the most prominent layer lines. The 2.44 nm layer lines indicate the pitch of the helical pili. Additional reference rings (4.25, 2.6, 1.77 and 1.16 nm) shown here aid comparison with classical pattern in C. Relevant features are boxed. (box 1) the equatorial intensity at 4.2 nm, (box 2) the 2.44 nm layer line, and (box 3) the 1.16 nm layer line. Boxes 2 and 3 have been enhanced for contrast. (c) Qualitative features of synchrotron-based fiber diffraction pattern collected from capillary aligned P pili from *E. coli* strain Cla-pRHU845. The same resolution guides as in panel (b) are shown

For amyloid fibrils the best diffracting images were averaged to produce 0.505 and 0.497 layer lines arising from b-strand stacking and an equatorial intensity is visible at 1.1 nm (Figure 6.5b) due to b-sheet stacking. These spacings indicate that amyloid fibrils are composed of β-sheets across the filament axis, similar to other amyloid structures[121,122].

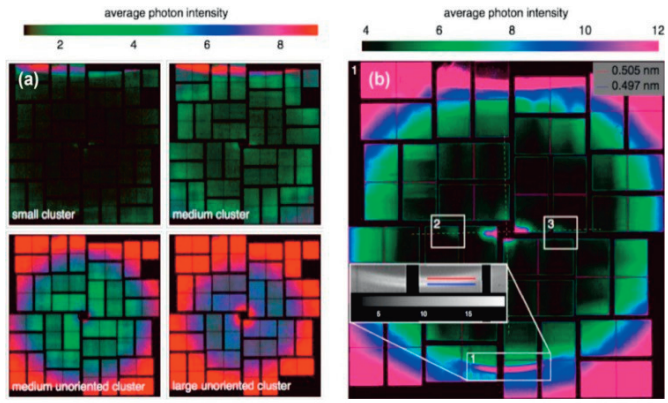

Figure 6.5: XFEL fiber diffraction from AgelN amyloid fibrils colored according to photon intensity per detector pixel. (a) Four XFEL fiber diffraction patterns from single femtosecond pulses of photons of X-ray wavelength 2.0664 Å. 66,270 such patterns were classified as either usable (small or medium cluster of aligned filaments) or unusable (medium, large non-oriented clusters of filaments). Only the most intense, usable patterns were selected and averaged. (b) An averaged XFEL fiber diffraction pattern from 48,747 images that shows the most prominent layer lines. (box 1) 0.505 and 0.497 nm meridional layer lines arising from the amyloid fibrils' b-strand stacking. The strong equatorial intensity in (Boxes 2 and 3) at 1.1 nm arises from b-sheet stacking. (Inset) An enlargement of the 0.505 and 0.497 nm meridional layer lines.

The final filament system studied was the α-synuclein fibril, a main component of Lewy bodies and associated with Parkinson's disease. Previous attempts with visible light microscopy proved to be difficult as the maximum width of the crystals is 200 nm which is too small for light microscopy and X-ray diffraction patterns obtained at Spring8 beamline 32XU revealed a 4.6 Å reflection.

During this experiment, we were able to achieve high resolution diffraction for the G11A sample made possible due to the combination of the GDVN injector and the XFEL source. The diffraction patterns obtained from this experiment varied from fiber diffraction (Figure 6.6a) to single crystal lattice (Figure 6.6b).

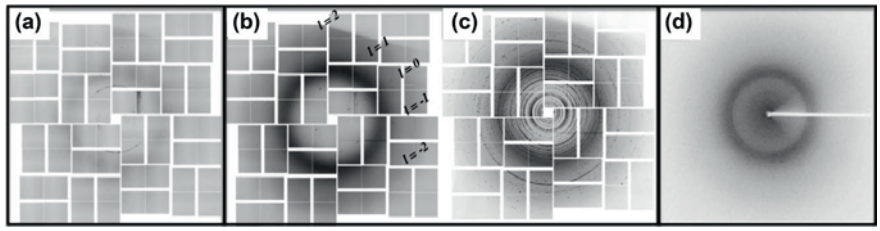

Figure 6.6: XFEL fiber diffraction from G11A aggregates. (a) An example of a single diffraction pattern from the most fibrillar aggregates. (b) An example of a single diffraction pattern from the most crystalline, single, G11A aggregates. The Miller indices are indicated. (c) A maximum projection computed using all diffraction patterns of a single run. (d) The best diffraction pattern that could be obtained using a 1.5 ln focus beam at a third-generation synchrotron and sample mounted in a loop

Figure 6.6C shows the maximum photon count per pixel on the CSPAD detector for all the diffraction patterns which is seen as a sharp reflection spread to form arcs. These sharp reflections tend to enhance the location of the bright peaks which allows us to differentiate those from diffuse scattering indicating the fibrils are crystalline aggregates. With enough images and appropriate sorting algorithns in the future we will be able to obtain three- dimensional crystal diffraction patterns.

6.4 Summary

In Paper IV, we performed single-shot fiber diffraction of about 100 filaments using a combination of liquid micro-jet and powerful femtosecond X-ray pulses. Using computational sorting algorithms, we sorted the best diffraction data which upon averaging provided improved fiber diffraction data. The results that the flow-aligned data can be further computationally aligned to a disorientation standard deviation of approximately 5 degrees. The combination of single filament and XFEL fiber diffraction methods has several advantages over classical fiber diffraction such as requiring less protein, difficult filament alignment protocols and an exciting possibility to obtain 3D diffraction data from single filaments.

6.5 Imaging Microtubules at an XFEL

During the same beamtime at LCLS in October 2013, we also performed XFEL imaging on microtubules. In Paper V we explore XFEL imaging of microtubules using a combination of the micro-jet[96], image sorting algorithms and merging them to obtain 2D diffraction patterns. From the data obtained in this experiment we show that the resolution can be extended to 2 nm. This data extending to 2 nm obtained from these 2D diffraction images was used to reconstruct a projection image of the microtubule.

6.5.1 Sample preparation

Tubulin samples were polymerized and stabilized using the anti-cancer agent taxol[123]. Taxol promotes the assembly of microtubules by reducing the critical concentration of tubulin required for polymerization *in*-vitro[124]. Additionally, taxol prevents the microtubules from disassembly under cold conditions[125]. Since the experiment was performed at room temperature it was vital to have stable microtubule while keeping disassembly as low as possible. The taxol-stabilized microtubule samples were then injected into a vacuum chamber where the sample was intercepted by a highly focused (~ 200 nm focal diameter) XFEL beam. The samples were delivered using a gas dynamic virtual nozzle[96,126].

6.5.2 Data collection

The experiment was performed at the Coherent X-ray Imaging (CXI) experimental station[45] of the Linac Coherent Light Source[89] at the SLAC National Accelerator laboratory. Each X-ray exposure contained approximately 2 mJ of energy, corresponding to approximately 2 x 10^{12} photons per pulse and was 33 fs in duration. The images were collected with a CSPAD detector[44] at a rate of 120 Hz .

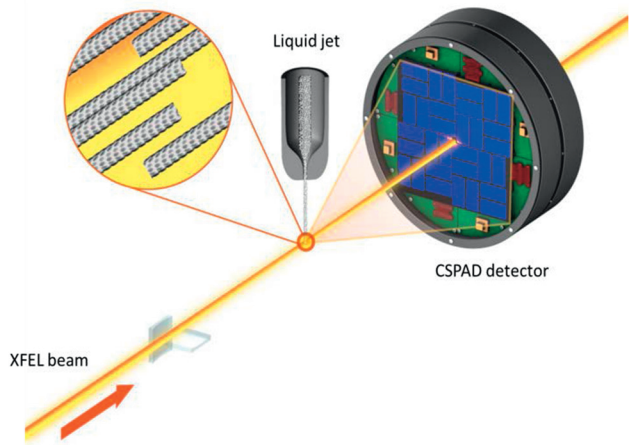

Figure 6.7: Schematic illustration of the experimental setup. Samples of pre-formed microtubules were injected across a focused X-ray free electron laser (XFEL) beam. Diffraction data were recorded on a CSPAD X-ray detector which was read out at 120 Hz, which matched the incoming repetition rate of the XFEL. Under the experimental conditions approximately twenty microtubules were intercepted by the X-ray beam as it passed through the microjet.

We used a protein concentration of 5 mg/ml which resulted in approximately 20 microtubules within a ~0.06 μm^3 volume which was intercepted by the XFEL beam. The microtubules were aligned to a high degree[48] and the X-ray scattering from every pulse contained scattering from approximately 20 polymers. As a result of the alignment we were able to see diffraction spots on individual detector images, characteristic of microtubule fibre diffraction (Figure 6.8A).

6.5.3 Data sorting and classification

An experiment at the LCLS produces millions of diffraction patterns which have to be carefully sorted out to obtain interpretable data. In this particular experiment we collected almost a million images in a single experimental shift (12 hours). The initial processing of the data was done with the Cheetah software package[127] and based on manual inspection of images from different collection runs 10% of those images were subjected to further analysis. Since the microtubule polymers are present in a buffer solution, there is a lot of background scattering from the solution and also scattering from the edge of the jet stream[128].

The images resulting from the background solution scattering as well the jet scattering has to be removed before further processing which resulted in 60 % of the images being discarded.

The next step was classifying those images according to the angle of the equatorial diffraction line relative to the detector geometry. The equatorial line corresponds to the perpendicular direction in a fiber diffraction pattern. Blocks of 1000 images were divided into five groups by class averaging[129] which resulted in an averaged diffraction pattern within each class with a layer-line visible at the 4 nm resolution (Figure 6.8B). Based on the contrast of the diffraction spots along the 4 nm layer line, the orientation of the equatorial line was determined which was then used as a marker to superimpose the class averaged images. All these superimposed images were then averaged revealing the high resolution 2 nm layer lines (Figure 6.8C). In the final step, data optimization was done with the averaged images (with visible 2 nm layer lines) images and along with the intense peaks which are similar to diffraction peaks, made it possible to fit the individual peaks with a horizontal and vertical Gaussian function (Figure 6.8D). Most of the noise arising out of the scattering from the solution, bad pixels in the detector etc., were removed in this step.

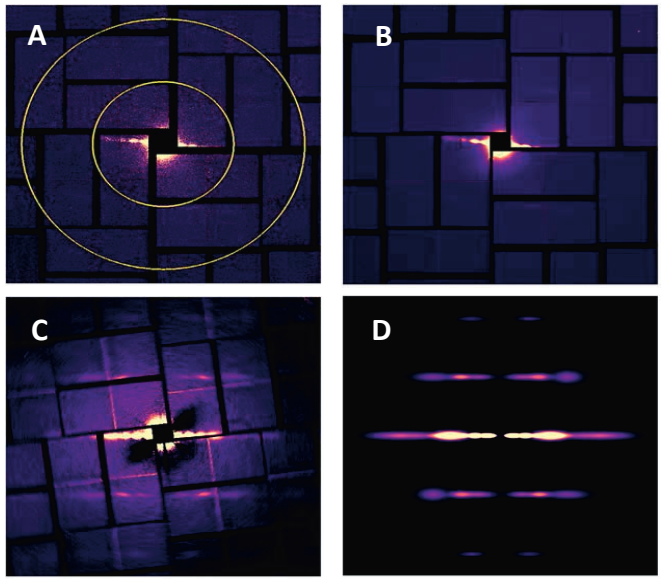

Figure 6.8: Diffraction images and class averages recovered from samples of microtubules. **A**, X-ray diffraction images from a single shot. **B**, Average of approximately 200 images recovered by class average sorting of the X-ray diffraction patterns using software originally developed for electron microscopy applications[1]. **C**, Sum of the class averages after aligning each class average by rotating about the beam centre. **D**, Fitted diffraction image recovered by fitting Gaussian peaks to the features identified as diffraction peaks in C.

The next step in the process is to recover the 2D projection images of a microtubule using the data shown in Figure 6.8 by a iterative phase retrieval algorithm implemented in MatLab. Figure 6.9 represents the results of this retrieval to recover the 2D projection images from each of the images in Figure 6.8.

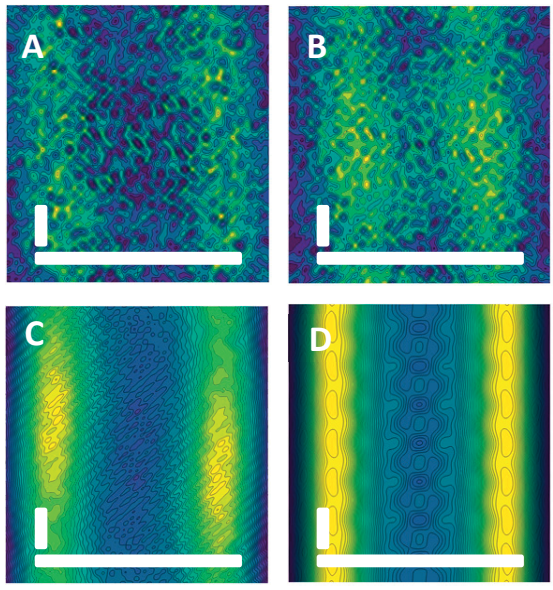

Figure 6.9: Results of iterative phase retrieval assuming that the electron density falls to zero outside of the microtubule. **A**, 2D projection image recovered after Fourier transform of the image in Fig. 6.8A using a homogeneous tube for initial phase and after 50 cycles of iterative phase retrieval. **B**, 2D projection image recovered after 50 cycles of iterative phase retrieval of the image shown in Fig 6.8B. **C**, 2D projection image recovered after 100 cycles of iterative phase retrieval of the image shown in Fig 6.8C. **D**, 2D projection image recovered after 150 cycles of iterative phase retrieval of the image shown in Fig 6.8D. After each imaging processing step, the resulting image shows increasing detail. Both the average microtubule diameter of 25 nm and sub-structures of 4 nm become visible when inverting the fitted diffraction image. White bars indicate 25 nm in the horizontal direction and 4 nm in the vertical direction. Blue represents low projection density whereas yellow is high projection density.

From Figure 6.8 it is clear that it is possible to obtain structural information concerning the microtubule diameter from just a single shot of the X-ray pulse and the information content improves after each subsequent step of image processing. Figure 6.8C represents the outcome when all class averages are aligned and merged together into a single image and in Figure 6.9C the borders of the microtubule become clearly defined after Fourier inversion with a diameter of 20 nm. The ''clean'' images (Figure6.8D) that were reconstructed from Gaussian fits to the X-ray diffraction spots visible in Figure 6.8C provides additional structural details. By looking at Figure 6.9C and 6.9D, one can already spot the

differences emerging from this approach. The boundary lines are more well defined and improved, and details corresponding to the monomer at 4 nm become visible after image reconstruction. The dimensions obtained by this method enable us to obtain structural information that is highly relevant biologically. The reconstructed images of the microtubules with a peak-to-peak separation of 20 nm are representative of microtubule mixture dominated by 14 protofilaments.

6.5.4 Summary

In PAPER V we performed coherent diffracting imaging of 20 microtubules in a single shot at a XFEL. By carefully sorting the X- ray diffraction data by adapting techniques from electron microscopy and by applying image reconstruction algorithms we were able to visualize structural details down to 2 nm resolution. In the future the goal would be to extend such high resolution diffractive imaging down to the single particle level.

It will also be interesting to study microtubule dynamic instability, a phenomenon in which microtubules grow and shrink which is inherent to their function and the critical role they play in several important cellular functions[43]. Advancements in sample delivery systems and improvements in XFEL technology like providing tighter X-ray pulses it will be possible to address challenging questions in biology.

Chapter 7

Concluding remarks

This thesis summarizes five years of research carried out during my PhD. The idea behind a major part of the work involved in this thesis was to invent a biophysical method to probe conformational dynamics in proteins using GHz frequency radiation with solution X-ray scattering studies. To perform these studies microtubules were chosen as the model system since they are relatively easy to purify in large amount and give a strong X- ray scattering signal. It is also an important system to study since they are involved in several crucial functions within the cytoskeleton including cellular communication, cell division among several other functions.

I began the quest towards achieving this goal by purifying proteins from bovine and porcine brains with already established purification protocols. The first part of the work described in this thesis (PAPER I) involved studying microtubule polymerization dynamics under the influence of microwaves. We built a set-up and after several iterations we were able to produce reliable and reproducible kinetic curves. Once a reliable experimental set-up and measurement protocol were established, we were able to show a functional effect in that microwaves at 20 GHz could accelerate the growth of microtubules. While this study lays the foundation for the effect of microwaves, we simultaneously performed solution X-ray scattering studies to see if microwaves induced any structural perturbations in microtubules (PAPER III).

We began this journey by re-engineering an underutilized crystallography beamline (PAPER II) at MaxLab (Max III) to perform WAXS measurements. What we did here was to

construct a WAXS set-up and validated the performance and reliability of the measurements with protein systems for which there was data available from other synchrotron sources. The system was successfully validated and we propose to use similar set-ups to perform proof-of-principle experiments to validate a new protein target and optimize experimental conditions for reaction initiation.

We extended the light scattering studies to solution X-ray scattering to probe for any structural perturbations (PAPER III) in microtubules under the influence of microwaves. These experiments were done at the Swiss Light Source (SLS) and we were able to measure reproducible difference signal in the SAXS region which was not due to thermal effects and the analysis of these results is ongoing.

We also performed Coherent Diffractive Imaging on fibers and filament systems at a XFEL (PAPER IV and PAPER V) using a Gas Dynamic Virtual Nozzle (GDVN) for sample delivery. Flow alignment of four different biological filament systems (PAPER IV) was demonstrated in a liquid microjet. Single-shot diffraction images of 100 filaments permitted computational selection of the best images which upon averaging improved the resolution of the fiber diffraction data. Similarly, we demonstrate flow alignment of microtubules (PAPER V) and performed an image reconstruction to obtain a projection of a microtubule from the 2D diffraction data. From the image reconstruction we were able to visualize structural details such as the 4 nm monomer within the microtubule. With developments in sample injection systems[126,130]and improved detectors it will be possible to obtain single-shot diffraction images of microtubules and other systems at room temperature.

The effect of microwaves on biological systems has been controversial[15,16,39] and to my knowledge there is no conclusive evidence yet. The outcome of results depends on several factors which leads to contradicting interpretations such as the choice of the biological system, experiments performed in-vivo or in-vitro, frequency domain and the measurement technique chosen to record the data. While some of the results could hold water, any comparison with each other, due to the variations mentioned above, makes it harder to interpret the data. We, in our research were certainly biased in choosing solution X-ray scattering as the method of choice to study the microwave induced structural perturbations in microtubules. But difference-WAXS/SAXS is a very well established and reliable method

to study protein structural changes[58,82,85,87,90,105,131], a method to which our lab has made significant contributions.

We have demonstrated that by using difference WAXS/SAXS we can produce a reproducible difference signal on exposure to microwaves. Further experiments are needed to characterize the difference signal and assign those changes to a structural response within the microtubule. If we can show that microwaves can trigger structural perturbations, it can be used as a generic method to initiate reactions in many non-light activated protein systems in biology.

Bibliography

1 Boldon, L., Laliberte, F. & Liu, L. Review of the fundamental theories behind small angle X-ray scattering, molecular dynamics simulations, and relevant integrated application. *Nano Reviews* **6**, 10.3402/nano.v3406.25661, doi:10.3402/nano.v6.25661 (2015).

2 Fröhlich, H. The extraordinary dielectric properties of biological materials and the action of enzymes. *Proceedings of the National Academy of Sciences of the United States of America* **72**, 4211-4215 (1975).

3 Fröhlich, H. Long-range coherence and energy storage in biological systems. *International Journal of Quantum Chemistry* **2**, 641-649, doi:10.1002/qua.560020505 (1968).

4 Rojavin, M. A. & Ziskin, M. C. Medical application of millimetre waves. *QJM : monthly journal of the Association of Physicians* **91**, 57-66 (1998).

5 Skresanov, V. N., Kas, I. V., Okhryamkina, E. A., Palamarchuk, V. P. & Tondy, L. D. in *Physics and Engineering of Millimeter and Sub-Millimeter Waves, 2001. The Fourth International Kharkov Symposium on.* 939-940 vol.932.

6 Pakhomov, A. G., Akyel, Y., Pakhomova, O. N., Stuck, B. E. & Murphy, M. R. Current state and implications of research on biological effects of millimeter waves: A review of the literature. *Bioelectromagnetics* **19**, 393-413, doi:10.1002/(SICI)1521-186X(1998)19:7<393::AID-BEM1>3.0.CO;2-X (1998).

7 Li, X. H. *et al. Millimeter wave in the treatment of acute radiation-induced cervical skin ulcers: A 2-month randomized controlled follow-up*. Vol. 12 (2008).

8 Markov, M. S. Expanding Use of Pulsed Electromagnetic Field Therapies. *Electromagnetic Biology and Medicine* **26**, 257-274, doi:10.1080/15368370701580806 (2007).

9 Usichenko, T. I. *et al.* Low-Intensity Electromagnetic Millimeter Waves for Pain Therapy. *Evidence-based Complementary and Alternative Medicine* **3**, 201-207, doi:10.1093/ecam/nel012 (2006).

10 Ramundo-Orlando, A. Effects of Millimeter Waves Radiation on Cell Membrane - A Brief Review. *Journal of Infrared, Millimeter, and Terahertz Waves* **31**, 1400-1411, doi:10.1007/s10762-010-9731-z (2010).

11 ZISKIN, M. C. in *BIOELECTROMAGNETICS Current Concepts: The Mechanisms of the Biological Effect of Extremely High Power Pulses* (eds Sinerik N. Ayrapetyan & Marko S. Markov) 241-251 (Springer Netherlands, 2006).

12 Anisimov, S. V., Tarasov, K. V. & Boheler, K. R. in *Cell Biology (Third Edition)* 103-112 (Academic Press, 2006).
13 Ryan, K. L., D'Andrea, J. A., Jauchem, J. R. & Mason, P. A. Radio frequency radiation of millimeter wave length: potential occupational safety issues relating to surface heating. *Health Phys* **78**, 170-181 (2000).
14 Park, C. & Rappaport, T. S. Short-Range Wireless Communications for Next-Generation Networks: UWB, 60 GHz Millimeter-Wave WPAN, And ZigBee. *Wireless Commun.* **14**, 70-78, doi:10.1109/mwc.2007.4300986 (2007).
15 Dawe, A. S. *et al.* A small temperature rise may contribute towards the apparent induction by microwaves of heat-shock gene expression in the nematode Caenorhabditis Elegans. *Bioelectromagnetics* **27**, 88-97, doi:10.1002/bem.20192 (2006).
16 de Pomerai, D. *et al.* Cell biology: Non-thermal heat-shock response to microwaves. *Nature* **405**, 417-418 (2000).
17 de Pomerai, D. I. *et al.* Microwave radiation can alter protein conformation without bulk heating. *FEBS Letters* **543**, 93-97, doi:https://doi.org/10.1016/S0014-5793(03)00413-7 (2003).
18 Frey, A. H. & Messenger, R. Human Perception of Illumination with Pulsed Ultrahigh-Frequency Electromagnetic Energy. *Science* **181**, 356 (1973).
19 Foster, K. R. & Finch, E. D. Microwave Hearing: Evidence for Thermoacoustic Auditory Stimulation by Pulsed Microwaves. *Science* **185**, 256 (1974).
20 Stocklin, P. L. & Stocklin, B. F. Possible microwave mechanisms of the mammalian nervous system. *TIT J Life Sci* **9**, 29-51 (1979).
21 Devyatkov, N. D. Influence of Millimeter-band Electromagnetic Radiation on Biological Objects. *Soviet Physics Uspekhi* **16**, 568 (1974).
22 Smolyanskaya, A. Z. & Vilenskaya, R. L. Effects of Millimeter-band Electromagnetic Radiation on the Functional Activity of Certain Genetic Elements of Bacterial Cells. *Soviet Physics Uspekhi* **16**, 571 (1974).
23 Kondrat'eva, V. F., Chistyakova, E. N., Shmakova, I. F., Ivanova, N. B. & Treskunov, A. A. Effects of Millimeter-band Radio Waves on Certain Properties of Bacteria. *Soviet Physics Uspekhi* **16**, 572 (1974).
24 Rachel, W. *et al.* The influence of high intensity terahertz radiation on mammalian cell adhesion, proliferation and differentiation. *Physics in Medicine & Biology* **58**, 373 (2013).
25 Bock, J. *et al.* Mammalian Stem Cells Reprogramming in Response

to Terahertz Radiation. *PLoS ONE* **5**, e15806, doi:10.1371/journal.pone.0015806 (2010).

26 Dyson, H. J. & Wright, P. E. Intrinsically unstructured proteins and their functions. **6**, 197, doi:10.1038/nrm1589 (2005).

27 Wright, P. E. & Dyson, H. J. Intrinsically Disordered Proteins in Cellular Signaling and Regulation. *Nature reviews. Molecular cell biology* **16**, 18-29, doi:10.1038/nrm3920 (2015).

28 Adair, R. K. Biophysical limits on athermal effects of RF and microwave radiation. *Bioelectromagnetics* **24**, 39-48, doi:10.1002/bem.10061 (2003).

29 Challis, L. J. Mechanisms for interaction between RF fields and biological tissue. *Bioelectromagnetics* **26**, S98-S106, doi:10.1002/bem.20119 (2005).

30 Binhi, V. N. & Rubin, A. B. Magnetobiology: The kT Paradox and Possible Solutions. *Electromagnetic Biology and Medicine* **26**, 45-62, doi:10.1080/15368370701205677 (2007).

31 Lednev, V. V. *Possible mechanism of the effect of weak magnetic fields on biosystems*. Vol. 12 (1991).

32 A. Belova, N., N. Ermakova, O., Ermakov, A., Z. Rojdestvenskaya, Y. & V. Lednev, V. *The bioeffects of extremely weak power-frequency alternating magnetic fields*. Vol. 27 (2007).

33 Belova, N. A. & Panchelyuga, V. A. Lednev's model: Theory and experiment. *Biophysics* **55**, 661-674, doi:10.1134/s0006350910040263 (2010).

34 Bohr, H. & Bohr, J. Microwave-enhanced folding and denaturation of globular proteins. *Physical Review E* **61**, 4310-4314 (2000).

35 Copty, A. *et al.* Probing of the microwave radiation effect on the green fluorescent protein luminescence in solution. *Synthetic Metals* **155**, 422-425, doi:https://doi.org/10.1016/j.synthmet.2005.09.028 (2005).

36 Copty, A. B., Neve-Oz, Y., Barak, I., Golosovsky, M. & Davidov, D. Evidence for a Specific Microwave Radiation Effect on the Green Fluorescent Protein. *Biophysical Journal* **91**, 1413-1423, doi:10.1529/biophysj.106.084111 (2006).

37 Porcelli, M. *et al.* Non-thermal effects of microwaves on proteins: thermophilic enzymes as model system. *FEBS Letters* **402**, 102-106, doi:https://doi.org/10.1016/S0014-5793(96)01505-0 (1997).

38 Mancinelli, F. *et al.* Non-thermal effects of electromagnetic fields at mobile phone frequency on the refolding of an intracellular protein: Myoglobin. *Journal of Cellular Biochemistry* **93**, 188-196, doi:10.1002/jcb.20164 (2004).

39 Retraction. *Nature* **440**, 437-437 (2006).

40 Burns, R. G. α-, β-, and γ-tubulins: Sequence comparisons and structural constraints. *Cell Motility and the Cytoskeleton* **20**, 181-189, doi:10.1002/cm.970200302 (1991).
41 Kirschner, M. & Mitchison, T. Beyond self-assembly: From microtubules to morphogenesis. *Cell* **45**, 329-342, doi:http://dx.doi.org/10.1016/0092-8674(86)90318-1 (1986).
42 Mitchison, T. & Kirschner, M. Dynamic instability of microtubule growth. *Nature* **312**, 237-242 (1984).
43 Desai, A. & Mitchison, T. J. MICROTUBULE POLYMERIZATION DYNAMICS. *Annual Review of Cell and Developmental Biology* **13**, 83-117, doi:10.1146/annurev.cellbio.13.1.83 (1997).
44 Hart, P. *et al.* The CSPAD megapixel x-ray camera at LCLS. *Proc Spie* **8504**, doi:Artn 85040c10.1117/12.930924 (2012).
45 Boutet, S. & Williams, G. J. The Coherent X-ray Imaging (CXI) instrument at the Linac Coherent Light Source (LCLS). *New J Phys* **12**, doi:Artn 03502410.1088/1367-2630/12/3/035024 (2010).
46 Barends, T. R. M. *et al.* Direct observation of ultrafast collective motions in CO myoglobin upon ligand dissociation. *Science* **350**, 445-450, doi:10.1126/science.aac5492 (2015).
47 Chapman, H. N. *et al.* Femtosecond X-ray protein nanocrystallography. *Nature* **470**, 73-77, doi:http://www.nature.com/nature/journal/v470/n7332/abs/10.1038-nature09750-unlocked.html#supplementary-information (2011).
48 Popp, D. *et al.* Flow-aligned, single-shot fiber diffraction using a femtosecond X-ray free-electron laser. *Cytoskeleton*, n/a-n/a, doi:10.1002/cm.21378.
49 Boutet, S. *et al.* High-resolution protein structure determination by serial femtosecond crystallography. *Science* **337**, 362-364, doi:10.1126/science.1217737 (2012).
50 Nogly, P. *et al.* Lipidic cubic phase injector is a viable crystal delivery system for time-resolved serial crystallography. **7**, 12314, doi:10.1038/ncomms12314 https://www.nature.com/articles/ncomms12314#supplementary-information (2016).
51 Johansson, L. C. *et al.* Structure of a photosynthetic reaction centre determined by serial femtosecond crystallography. **4**, 2911, doi:10.1038/ncomms3911 https://www.nature.com/articles/ncomms3911#supplementary-information (2013).
52 Cartlidge, E. European XFEL to shine as brightest, fastest x-ray source. *Science* **354**, 22-23, doi:10.1126/science.354.6308.22

(2016).
53 Andreas, K., Markus, K., Jolanta, S.-D. & Monica, T. Detector Development for the European XFEL: Requirements and Status. *Journal of Physics: Conference Series* **425**, 062013 (2013).
54 Nagaya, K. *et al.* Femtosecond charge and molecular dynamics of I-containing organic molecules induced by intense X-ray free-electron laser pulses. *Faraday Discussions* **194**, 537-562, doi:10.1039/C6FD00085A (2016).
55 Motomura, K. *et al.* Electronic decay and fragmentation dynamics of iodomethane, multiply core-ionized by photoabsorption of intense XFEL pulses. *Journal of Physics: Conference Series* **488**, 032043 (2014).
56 Neutze, R., Wouts, R., van der Spoel, D., Weckert, E. & Hajdu, J. Potential for biomolecular imaging with femtosecond X-ray pulses. *Nature* **406**, 752-757 (2000).
57 Dmitri, I. S. & Michel, H. J. K. Small-angle scattering studies of biological macromolecules in solution. *Reports on Progress in Physics* **66**, 1735 (2003).
58 Westenhoff, S. *et al.* Rapid readout detector captures protein time-resolved WAXS. *Nature Methods* **7**, 775, doi:10.1038/nmeth1010-775chttps://www.nature.com/articles/nmeth1010-775c#supplementary-information (2010).
59 Petoukhov, M. V., Konarev, P. V., Kikhney, A. G. & Svergun, D. I. ATSAS 2.1 - towards automated and web-supported small-angle scattering data analysis. *Journal of Applied Crystallography* **40**, s223-s228, doi:doi:10.1107/S0021889807002853 (2007).
60 V. Konarev, P., V. Petoukhov, M. & I. Svergun, D. *MASSHA – A Graphic System for Rigid Body Modelling of Macromolecular Complexes Against Solution Scattering Data*. Vol. 34 (2001).
61 Svergun, D. I. Restoring low resolution structure of biological macromolecules from solution scattering using simulated annealing. *Biophysical Journal* **76**, 2879-2886 (1999).
62 Hirai, M., Iwase, H., Hayakawa, T., Miura, K. & Inoue, K. *Structural hierarchy of several proteins observed by wide-angle solution scattering*. Vol. 9 (2002).
63 Makowski, L. Characterization of Proteins with Wide-angle X-ray Solution Scattering (WAXS). *Journal of structural and functional genomics* **11**, 9-19, doi:10.1007/s10969-009-9075-x (2010).
64 Borisy, G. G., Marcum, J. M., Olmsted, J. B., Murphy, D. B. & Johnson, K. A. PURIFICATION OF TUBULIN AND ASSOCIATED HIGH MOLECULAR WEIGHT PROTEINS FROM PORCINE BRAIN AND CHARACTERIZATION OF MICROTUBULE ASSEMBLY IN VITRO*.

Annals of the New York Academy of Sciences **253**, 107-132, doi:10.1111/j.1749-6632.1975.tb19196.x (1975).

65 Howard, J. & Hyman, A. A. in *Methods in Cell Biology* Vol. 39 (ed Jonathan M. Scholey) 105-113 (Academic Press, 1993).

66 Castoldi, M. & Popov, A. V. Purification of brain tubulin through two cycles of polymerization-depolymerization in a high-molarity buffer. *Protein Expr Purif* **32**, 83-88, doi:10.1016/S1046-5928(03)00218-3 (2003).

67 Kuznetsov, S. A. & Gelfand, V. I. in *Kinesin Protocols* (ed Isabelle Vernos) 1-7 (Humana Press, 2001).

68 Ashford, A. J. & Hyman, A. A. in *Cell Biology (Third Edition)* 155-160 (Academic Press, 2006).

69 Voter, W. A. & Erickson, H. P. The kinetics of microtubule assembly. Evidence for a two-stage nucleation mechanism. *Journal of Biological Chemistry* **259**, 10430-10438 (1984).

70 Erickson, H. P. Assembly of microtubules from preformed, ring-shaped protofilaments and 6-s tubulin. *Journal of Supramolecular Structure* **2**, 393-411, doi:10.1002/jss.400020228 (1974).

71 Kirschner, M. W., Williams, R. C., Weingarten, M. & Gerhart, J. C. Microtubules from Mammalian Brain: Some Properties of Their Depolymerization Products and a Proposed Mechanism of Assembly and Disassembly. *Proceedings of the National Academy of Sciences* **71**, 1159-1163 (1974).

72 Johnson, K. A. & Borisy, G. G. Kinetic analysis of microtubule self-assembly in vitro. *Journal of Molecular Biology* **117**, 1-31, doi:https://doi.org/10.1016/0022-2836(77)90020-1 (1977).

73 Putnam, C. D., Hammel, M., Hura, G. L. & Tainer, J. A. X-ray solution scattering (SAXS) combined with crystallography and computation: defining accurate macromolecular structures, conformations and assemblies in solution. *Q Rev Biophys* **40**, doi:10.1017/s0033583507004635 (2007).

74 Förster, F. *et al.* Integration of small-angle X-ray scattering data into structural modeling of proteins and their assemblies. *J Mol Biol* **382**, doi:10.1016/j.jmb.2008.07.074 (2008).

75 Chacón, P., Díaz, J. F., Morán, F. & Andreu, J. M. Reconstruction of protein form with X-ray solution scattering and a genetic algorithm11Edited by R. Huber. *Journal of Molecular Biology* **299**, 1289-1302, doi:https://doi.org/10.1006/jmbi.2000.3784 (2000).

76 Svergun, D. I., Petoukhov, M. V. & Koch, M. H. Determination of domain structure of proteins from X-ray solution scattering. *Biophys J* **80**, doi:10.1016/s0006-3495(01)76260-1 (2001).

77 <SAXS_Basics.pdf>.

78 <x-ray-scattering-basics-roessle.pdf>.
79 Svergun, D., Barberato, C. & Koch, M. H. J. CRYSOL - a Program to Evaluate X-ray Solution Scattering of Biological Macromolecules from Atomic Coordinates. *Journal of Applied Crystallography* **28**, doi:10.1107/s0021889895007047 (1995).
80 Bardhan, J., Park, S. & Makowski, L. SoftWAXS: a computational tool for modeling wide-angle X-ray solution scattering from biomolecules. *Journal of Applied Crystallography* **42**, doi:10.1107/s0021889809032919 (2009).
81 Park, S., Bardhan, J. P., Roux, B. & Makowski, L. Simulated x-ray scattering of protein solutions using explicit-solvent models. *J Chem Phys* **130**, doi:10.1063/1.3099611 (2009).
82 Andersson, M. *et al.* Structural Dynamics of Light-Driven Proton Pumps. *Structure* **17**, 1265-1275, doi:https://doi.org/10.1016/j.str.2009.07.007 (2009).
83 Cammarata, M. *et al.* Tracking the structural dynamics of proteins in solution using time-resolved wide-angle X-ray scattering. *Nature methods* **5**, 881-886, doi:10.1038/nmeth.1255 (2008).
84 Ramachandran, P. L. *et al.* The Short-Lived Signaling State of the Photoactive Yellow Protein Photoreceptor Revealed by Combined Structural Probes. *Journal of the American Chemical Society* **133**, 9395-9404, doi:10.1021/ja200617t (2011).
85 Malmerberg, E. *et al.* Time-Resolved WAXS Reveals Accelerated Conformational Changes in Iodoretinal-Substituted Proteorhodopsin. *Biophysical Journal* **101**, 1345-1353, doi:10.1016/j.bpj.2011.07.050 (2011).
86 Ahn, S., Kim, K. H., Kim, Y., Kim, J. & Ihee, H. Protein Tertiary Structural Changes Visualized by Time-Resolved X-ray Solution Scattering. *The Journal of Physical Chemistry B* **113**, 13131-13133, doi:10.1021/jp906983v (2009).
87 Takala, H. *et al.* Signal amplification and transduction in phytochrome photosensors. *Nature* **509**, 245-248, doi:10.1038/nature13310 (2014).
88 Cho, H. S. *et al.* Protein structural dynamics in solution unveiled via 100-ps time-resolved x-ray scattering. *Proceedings of the National Academy of Sciences of the United States of America* **107**, 7281-7286, doi:10.1073/pnas.1002951107 (2010).
89 EmmaP *et al.* First lasing and operation of an angstrom-wavelength free-electron laser. *Nat Photon* **4**, 641-647 (2010).
90 Arnlund, D. *et al.* Visualizing a protein quake with time resolved X-ray scattering at a free electron laser. *Nature methods* **11**, 923-926, doi:10.1038/nmeth.3067 (2014).

91 Levantino, M. *et al.* Ultrafast myoglobin structural dynamics observed with an X-ray free-electron laser. **6**, 6772, doi:10.1038/ncomms7772 https://www.nature.com/articles/ncomms7772#supplementary-information (2015).

92 Liang, M. *et al.* The Coherent X-ray Imaging instrument at the Linac Coherent Light Source. *Journal of Synchrotron Radiation* **22**, 514-519, doi:doi:10.1107/S160057751500449X (2015).

93 Seibert, M. M. *et al.* Single mimivirus particles intercepted and imaged with an X-ray laser. *Nature* **470**, 78-81, doi:10.1038/nature09748 (2011).

94 Ekeberg, T. *et al.* Three-dimensional reconstruction of the giant mimivirus particle with an x-ray free-electron laser. *Phys Rev Lett* **114**, 098102, doi:10.1103/PhysRevLett.114.098102 (2015).

95 van der Schot, G. *et al.* Imaging single cells in a beam of live cyanobacteria with an X-ray laser. *Nature Communications* **6**, doi:ARTN 5704 10.1038/ncomms6704 (2015).

96 DePonte, D. P. *et al.* Gas dynamic virtual nozzle for generation of microscopic droplet streams. *Journal of Physics D: Applied Physics* **41**, 195505 (2008).

97 Weierstall, U. Liquid sample delivery techniques for serial femtosecond crystallography. *Philosophical Transactions of the Royal Society B: Biological Sciences* **369**, doi:10.1098/rstb.2013.0337 (2014).

98 Landau, E. M. & Rosenbusch, J. P. Lipidic cubic phases: A novel concept for the crystallization of membrane proteins. *Proceedings of the National Academy of Sciences* **93**, 14532-14535 (1996).

99 Johansson, L. C., Stauch, B., Ishchenko, A. & Cherezov, V. A Bright Future for Serial Femtosecond Crystallography with XFELs. *Trends in Biochemical Sciences* **42**, 749-762, doi:https://doi.org/10.1016/j.tibs.2017.06.007 (2017).

100 Caffrey, M. A comprehensive review of the lipid cubic phase or in meso method for crystallizing membrane and soluble proteins and complexes. *Acta Crystallographica Section F* **71**, 3-18, doi:doi:10.1107/S2053230X14026843 (2015).

101 Ursby, T. *et al.* The New Macromolecular Crystallography Stations At MAX-lab: The MAD Station. *AIP Conference Proceedings* **705**, 1241-1246 (2004).

102 Ursby, T. *et al.* The macromolecular crystallography beamline I911-3 at the MAX IV laboratory. *Journal of Synchrotron Radiation* **20**, 648-653, doi:10.1107/S0909049513011734 (2013).

103 Dubuisson, J.-M. D., Thierry; Vachette, Patrice. Improved Signal-to-

Background Ratio in Small-Angle X-ray Scattering Experiments with Synchrotron Radiation using an Evacuated Cell for Solutions. *Journal of Applied Crystallography* **30**, 49-54 (1997).

104 Clement E. Blanchet, A. V. Z., Alexey G. Kikhney, Daniel Franke, Peter V. Konarev, Weifeng Shang, Robbert Klaering, Bernd Robrahn, Christoph Hermes, Florent Cipriani, Dmitri I. Svergun and Manfred Roessle. Instrumental setup for high-throughput small- and wide-angle solution scattering at the X33 beamline of EMBL Hamburg. *J. Appl. Cryst.* **45**, 489-495, doi:10.1107/S0021889812013490 (2012).

105 Björling, A. *et al.* Ubiquitous Structural Signaling in Bacterial Phytochromes. *The Journal of Physical Chemistry Letters* **6**, 3379-3383, doi:10.1021/acs.jpclett.5b01629 (2015).

106 Ellis-Davies, G. C., Kaplan, J. H. & Barsotti, R. J. Laser photolysis of caged calcium: rates of calcium release by nitrophenyl-EGTA and DM-nitrophen. *Biophysical Journal* **70**, 1006-1016 (1996).

107 Kaplan, J. H. & Somlyo, A. P. Flash photolysis of caged compounds: New tools for cellular physiology. *Trends in Neurosciences* **12**, 54-59, doi:https://doi.org/10.1016/0166-2236(89)90136-7 (1989).

108 Ayer, R. K. & Zucker, R. S. Magnesium binding to DM-nitrophen and its effect on the photorelease of calcium. *Biophysical Journal* **77**, 3384-3393 (1999).

109 Brown, E. B., Shear, J. B., Adams, S. R., Tsien, R. Y. & Webb, W. W. Photolysis of caged calcium in femtoliter volumes using two-photon excitation. *Biophysical Journal* **76**, 489-499 (1999).

110 Polanyi, M. & Weissenberg, K. Das Röntgen-Faserdiagramm. *Zeitschrift für Physik* **9**, 123-130, doi:10.1007/bf01326961 (1922).

111 Polanyl, M. Das Röntgen-Faserdiagramm. *Zeitschrift für Physik* **7**, 149-180, doi:10.1007/bf01332786 (1921).

112 Franklin, R. E. & Gosling, R. G. Molecular Configuration in Sodium Thymonucleate. *Nature* **171**, 740-741 (1953).

113 Watson, J. D. & Crick, F. H. C. Molecular Structure of Nucleic Acids: A Structure for Deoxyribose Nucleic Acid. *Nature* **171**, 737-738 (1953).

114 Wilkins, M. H. F., Stokes, A. R. & Wilson, H. R. Molecular Structure of Nucleic Acids: Molecular Structure of Deoxypentose Nucleic Acids. *Nature* **171**, 738-740 (1953).

115 Holmes, K. C. & Blow, D. M. in *Methods of Biochemical Analysis* 113-239 (John Wiley & Sons, Inc., 2006).

116 Arnott, S. in *Fiber Diffraction Methods* Vol. 141 *ACS Symposium Series* Ch. 1, 1-30 (AMERICAN CHEMICAL SOCIETY, 1980).

117 Toshiro, O., Iwasa, M., Aihara, T., Maéda, Y. & Narita, A. *The nature*

of the globular- to fibrous-actin transition. Vol. 457 (2009).

118 Yamashita, I., Suzuki, H. & Namba, K. Multiple-step method for making exceptionally well-oriented liquid-crystalline sols of macromolecular assemblies11Edited by K. Nagai. *Journal of Molecular Biology* **278**, 609-615, doi:https://doi.org/10.1006/jmbi.1998.1710 (1998).

119 Popp, D., Lednev, V. V. & Jahn, W. Methods of preparing well-orientated sols of f-actin containing filaments suitable for X-ray diffraction. *Journal of Molecular Biology* **197**, 679-684, doi:https://doi.org/10.1016/0022-2836(87)90474-8 (1987).

120 Holmes, K. C., Popp, D., Gebhard, W. & Kabsch, W. Atomic model of the actin filament. *Nature* **347**, 44, doi:10.1038/347044a0 (1990).

121 Geddes, A. J., Parker, K. D., Atkins, E. D. T. & Beighton, E. "Cross-β" conformation in proteins. *Journal of Molecular Biology* **32**, 343-358, doi:https://doi.org/10.1016/0022-2836(68)90014-4 (1968).

122 Wille, H. *et al.* Natural and synthetic prion structure from X-ray fiber diffraction. *Proceedings of the National Academy of Sciences* **106**, 16990-16995, doi:10.1073/pnas.0909006106 (2009).

123 Dumontet, C. & Jordan, M. A. Microtubule-binding agents: a dynamic field of cancer therapeutics. *Nat Rev Drug Discov* **9**, 790-803, doi:10.1038/nrd3253 (2010).

124 Weaver, B. A. How Taxol/paclitaxel kills cancer cells. *Molecular Biology of the Cell* **25**, 2677-2681, doi:10.1091/mbc.E14-04-0916 (2014).

125 Schiff, P., Fant, J. & Horwitz, S. *Promotion of Microtubule Assembly in vitro by Taxol*. Vol. 277 (1979).

126 Weierstall, U., C H Spence, J. & B Doak, R. *Injector for scattering measurements on fully solvated biospecies*. Vol. 83 (2012).

127 Barty, A. *et al.* Cheetah: software for high-throughput reduction and analysis of serial femtosecond X-ray diffraction data. *Journal of Applied Crystallography* **47**, 1118-1131, doi:10.1107/S1600576714007626 (2014).

128 Scheres, S. H., Nunez-Ramirez, R., Sorzano, C. O., Carazo, J. M. & Marabini, R. Image processing for electron microscopy single-particle analysis using XMIPP. *Nat Protoc* **3**, 977-990, doi:10.1038/nprot.2008.62 (2008).

129 Scheres, S. H. *et al.* Maximum-likelihood multi-reference refinement for electron microscopy images. *J Mol Biol* **348**, 139-149, doi:10.1016/j.jmb.2005.02.031 (2005).

130 Hunter, M. S. *et al.* Fixed-target protein serial microcrystallography with an x-ray free electron laser. *Scientific Reports* **4**, 6026,

doi:10.1038/srep06026
https://www.nature.com/articles/srep06026#supplementary-information (2014).

131 Berntsson, O. *et al.* Sequential conformational transitions and alpha-helical supercoiling regulate a sensor histidine kinase. *Nat Commun* **8**, 284, doi:10.1038/s41467-017-00300-5 (2017).